Physical and Chemical Mechanisms of Lubricant Removal

During Stage I of the Sintering Process

A Thesis

Submitted to the Faculty

of the

WORCESTER POLYTECHNIC INSTITUTE

in partial fulfillment of the requirements for the
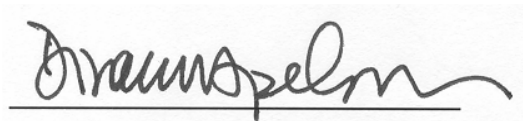
Degree of Master of Science

in

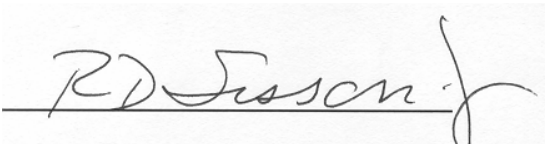Materials Science and Engineering

April 2006

By

Arnaud Gateaud

_____

APPROVED:

_____

Diran Apelian, Howmet Professor of Mechanical Engineering, Advisor

_____

Richard D. Sisson, Jr., George F. Fuller Professor of Mechanical Engineering
Materials Science & Engineering Program Director
Manufacturing Engineering Program Director

Abstract

The present study focuses on the physical and chemical mechanisms of lubricant removal during the first step of the sintering process during powder metallurgy (P/M) processing of ferrous systems.

Previous works on the kinetics of delubrication made it possible to develop an empirical model which accounts for the typical weight loss profile observed upon heating of green compacts. It has been established that the rate at which the parts are heated dictates the overall process kinetics, and fitting curve methods yield two parameters which contain the corresponding information: *(i)* T_{MAX} is the temperature of 50% lubricant removal, and *(ii)* b is representative of the slope of the curve during weight loss stage. Phase I of this study aims at determining the dependencies of these two parameters with respect to a series of physical variables: green density of the compacts; presence of an alloying element potentially catalytic for the reaction of lubricant pyrolysis; and procedure of compaction and geometry of the compacts. Also, it is suggested that the two parameters obtained from the fitting curve methods can be related to the main two mechanisms of delubrication: evaporation of the lubricant and conversion of the lubricant molecules into smaller hydrocarbons, assuming that these two mechanisms are the kinetically limiting mechanisms.

Furthermore, recent studies of the delubrication process have been opening the way to the potential development of gas sensors, which could eventually allow the direct monitoring of the emissions of gaseous species. Several key features have been reported in the literature, including a peak emission of hydrocarbons at the delubrication temperature, as well as strong emissions of CO and CO_2 at temperatures above 700°C. The scope of Phase II of this project was thus to verify that these features were retained under various processing conditions, so that the development of a sensor suitable for various sintering environments is viable. Variations in the emission profiles of gaseous species were observed as the processing conditions were changed, and when possible, potential justifications for these changes have been proposed.

Acknowledgements

Table of contents

List of Figures & Tables

—————————————————

1.0 Objectives

PHASE I

- Extend the empirical model of delubrication to warm-compacted parts.

- Establish the dependencies of lubricant removal kinetics with respect to green density, geometry and alloy composition of P/M compacts.

- Establish whether or not lubricant removal can be promoted by the presence of a potentially catalytic alloying element (i.e., nickel)

PHASE II

- Identify more extensively the gaseous species emitted during decomposition of EBS

- Identify the changes in gaseous species emission profiles as the processing conditions are modified, in order to ascertain the possibility of sensor development for online process control.

2.0 Physical Mechanisms of Delubrication

2.1 Introduction

Lubricants are known to be widely used during manufacturing of P/M components, as additives to the metal powders, in order to ease die ejection and reduce die wear [1, 2]. This phenomenon proceeds essentially by a reduction of interparticle and die/particle friction forces.

The drawback of this method stems from the fact that the green parts retain most of the lubricant after die ejection, requiring as a result proper lubricant removal. Delubrication is thus achieved by heating steadily the green compacts to temperatures as high as 900°C. Should the lubricant (typically a long-chain hydrocarbon) dwell inside the compacts until they enter the hot zone of the sintering furnace, its constitutive molecules would undergo rapid decomposition with subsequent gas expansion, thereby causing the formation of internal cracks. This problem is referred to as 'blistering'.

Other problems can result from the use of inappropriate processing conditions, such as carbon deposition inside or on the surface of the compacts, associated with localized carburization [3, 4], dimensional changes of the parts [5], and even decrease in the corrosion resistance of the end product [6]. However, the main concern of the delubrication process control remains to be able to predict when removal of the lubricant is complete (in terms of distance reached inside the sintering furnace, parts temperature, etc.)

Among the techniques that can be used to study delubrication, thermogravimetric analysis (TGA) is the one giving the best insight of the process kinetics. Typical TGA curves, for which sample weight is plotted as a function of temperature, consistently exhibit a sigmoidal profile. An empirical model developed and validated by Saha & Apelian [7-10] accounts for this weight loss profile, by using only two parameters dependent on the processing conditions and the lubricant used.

$$\alpha = \left(1 + \left(\frac{T}{T_{MAX}}\right)^b\right)^{-1} \tag{1}$$

In the above formula, α is the weight fraction of remaining lubricant inside the compact, T is the temperature of the part, T_{MAX} (first parameter) is the temperature of 50% lubricant removal, and b (second parameter) is representative of the slope of the curve during the weight loss stage: the higher b, the steeper the curve. *Figure 1* indicates, on a typical delubrication weight loss curve, what T_{MAX} and b correspond to.
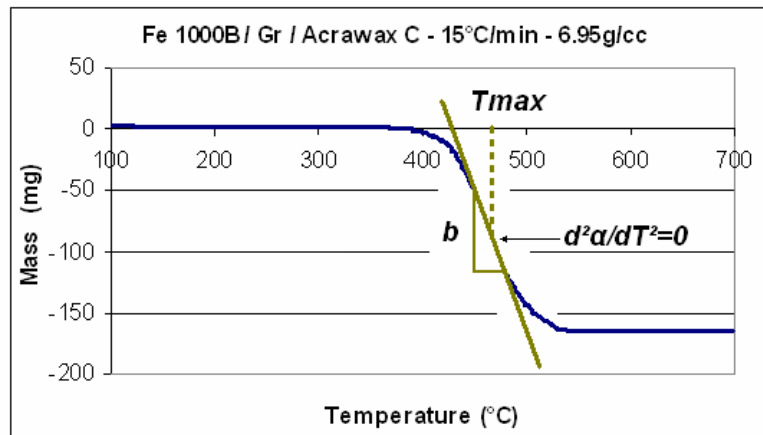
Figure 1. Delubrication of a Fe 1000B/Graphite/Acrawax C (0.6% wt) compact.
Heating rate: 15°C/min. Atmosphere: 5% hydrogen, 95% nitrogen. Flow rate of gases: 80 ml/min.
Schematic representation of the parameters b and T_{MAX}.

The above approach is useful since once the processing conditions (heating rate, atmosphere composition, flow rate of gases, water content) have been gauged and reproduced during TGA experiments, all the information relative to the kinetics of the process is contained in the two parameters b and T_{MAX}. It becomes then possible to predict, under the same conditions, the amount of lubricant removed from the parts for a certain temperature. The temperature of 97% removal can, for instance, be selected as an indicator of delubrication completion.

The relative effects of moisture content, hydrogen content, flow rate of gases and heating rate were evaluated [7, 8]. The rate at which green compacts are heated turns out to dictate the overall kinetics of delubrication. However, previous studies have not addressed the effect of alloy composition on the kinetics of lubricant decomposition and removal. Also, the dependencies of T_{MAX} and b, with respect to compact green density have not been established over an extended

range of densities, and the impact of compaction procedure (cold or warm) was never taken into consideration. Consequently, the purpose of this work is to study the impact of the parameters mentioned above on the kinetics of lubricant, as well as that of compact geometry. The choice of the presence of nickel as the varying factor of alloy composition is based on its known capacity to act as a catalyst in various reactions. Nickel has been identified as an alloying element potentially causing changes in the delubrication behaviour of PM compacts [11].

Finally, to confirm the assumption, according to which the parameter T_{MAX} would be representative of an overall evaporation temperature of the lubricant and the by-products of its early stages of decomposition, while b would relate to the kinetics of hydrocarbon decomposition [12].

2.2 Experimental Procedures

2.2.1 Alloy Composition

Three different alloy compositions are used in order to investigate the effect of Nickel on the kinetics of delubrication. The reference alloy composition consisted of 99.1% wt Ancorsteel Fe 1000B, admixed with 0.3% wt As3203 graphite and 0.6% wt lubricant (either Acrawax C or Ancormax D). Two Nickel-containing systems are used. The first one consists of 97.25% wt Ancorsteel Fe 1000B, 0.3% wt As3203 graphite, and 0.6% wt lubricant, admixed with 1.85% wt Nickel (Inco Ni 123). The second one is a Fe-Ni prealloyed system, consisting of 99.1% wt Ancorsteel 4600V, 0.3% wt As3203 graphite and 0.6% wt lubricant (the 4600V powder containing 1.83% wt Nickel). *Table 1* gives the alloy content for Fe 1000B and 4600V powders [13, 14]. *Figure 2* shows schematically the difference between prealloyed and admixed iron/nickel powders.

WEIGHT (%)	C	O	Mo	Mn	Cr	Cu	Ni
Fe 1000B	<0.01	0.09	---	0.10	0.03	0.05	0.05
4600V	0.01	0.13	0.56	0.15	---	---	1.83

Table 1. Alloy composition for Fe 1000B and 4600V [13, 14].

For the experiments relative to the presence of nickel and to compact geometry, two lubricants are used for each alloy composition: Acrawax C, a commonly used lubricant, and Ancormax D, used in the industry to produce high density components. Each compact contains initially 0.6% weight lubricant.
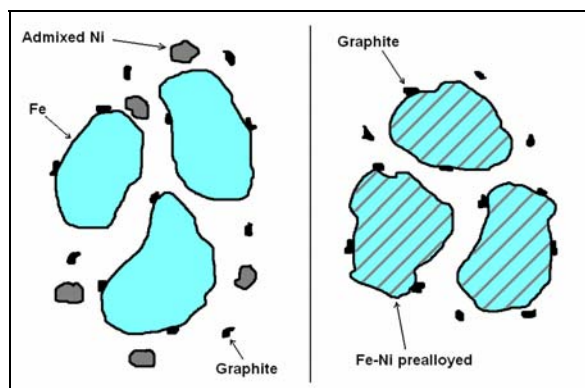
Figure 2. Schematic difference between admixed and prealloyed iron/nickel powders.

2.2.2 Compaction procedure

All compacts weight 29.0 grams, in order to eliminate the effect of compact size on the kinetics of lubricant removal. Regular cold compaction is performed to produce Acrawax C-lubricated parts, whereas a special procedure of warm compaction is used for Ancormax D-lubricated samples: the die is heated up to ca. 65°C and after filling, the powder stays for 2 minutes in the die before compaction. This procedure enhances powder compressibility, and allows the use of lower compaction pressures to achieve a given green density [15].

2.2.3 Green densities & geometries used

Table 2 summarizes the range of green densities covered during the study of the effect of this parameter. Acrawax C-lubricated compacts are pressed to densities ranging from 86.6% to 91.8% full density, whereas Ancormax D-lubricated compacts' green densities range from 90.5% to 94.3% full density. Compacts are prepared in a 32mm*13mm rectangular die, designed for TRS bars. The same compact geometry is used during the study of the effect of nickel.

	AW	*AW*	*AW*	*AW* *maxD*	*AW* *maxD*	*maxD*	*maxD*
Actual density (g.cm-3)	6.75	6.85	6.95	7.05	7.15	7.25	7.35
Theoretical density (% full)	86.6	87.9	89.2	90.5	91.8	93	94.3

Table 2. Range of green densities covered.
(AW stands for Acrawax C-lubricated, maxD for Ancormax D-lubricated).

In order to investigate the effect of compact geometry (surface/volume ratio), a cylindrical compact geometry is used (8mm*25.5mmØ). Both rectangular and cylindrical samples weight 29.0 grams.

2.2.4 TGA experimental procedure

The machine used for the thermogravimetric analysis is a Thermo Cahn 131. Samples were held in a 33mm*20mmØ cylindrical ceramic crucible. The dynamic range of the TGA machine being ±10.0 grams, a 25.0 grams counterweight is used for all the experiments.

Pure Helium is used as the purge gas to flow through the head of the TGA machine, at a rate of 90ml/min. The reaction atmosphere is a mixture of 5% Hydrogen in a balance of Nitrogen, and is flown at 80 ml/min, from the bottom of the quartz reactor tube; the exhaust vent being located ca. 10cm above the top of the ceramic crucible. The flow-meters (Cole-Parmer 032-41) used to monitor the flow rate of gases are calibrated, based on pure helium calibration charts for the purge gas, and pure nitrogen calibration charts for the atmosphere mixture.

Three different heating rates (5°C/min, 10°C/min and 15°C/min) are used during the experiments, so that subsequent statistical analysis can determine whether or not an interaction exists between the presence of Nickel inside the compact and the rate at which samples are heated up from 100°C to 700°C. The sampling time for data acquisition is 5 seconds, i.e. the part weight is recorded every 5 seconds.

Before each run, the quartz reactor tube is purged for 30 minutes with the hydrogen-nitrogen mixture, at a flow rate of 80ml/min, in order to eliminate any remaining moisture or oxygen from the atmosphere. Two runs are performed for each experimental condition being investigated.
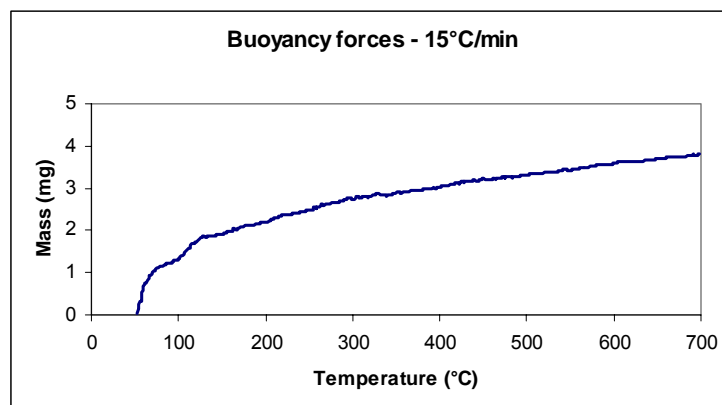
Figure 3. Weight evolution profile with inert sample / Effect of Buoyancy forces

7

2.2.5 Correction for Buoyancy forces

Since the reaction atmosphere inside the quartz reactor tube is submitted to gas expansion upon heating, all measurements are corrected for buoyancy forces. The method used here to determine the specific effect of buoyancy forces is to replace the iron green compacts by an inert sample having a similar volume. Samples are thus replaced by a 34mm*11mmØ glass rod and TGA runs were then performed under the same experimental conditions. A characteristic weight evolution profile is obtained for each heating rate and is subsequently subtracted from the data obtained during the actual experimental runs. *Figure 3* shows a weight evolution curve obtained in this manner, for a 15°C/min heating rate.

2.3 Results & Discussion

A preliminary result of this work is that the empirical model used here has been extended and validated for warm-compacted P/M compacts. *Figure 4* shows an excellent fit between experimental and theoretical curves for the removal of Ancormax D from a Fe-C compact, at 10°C/min.
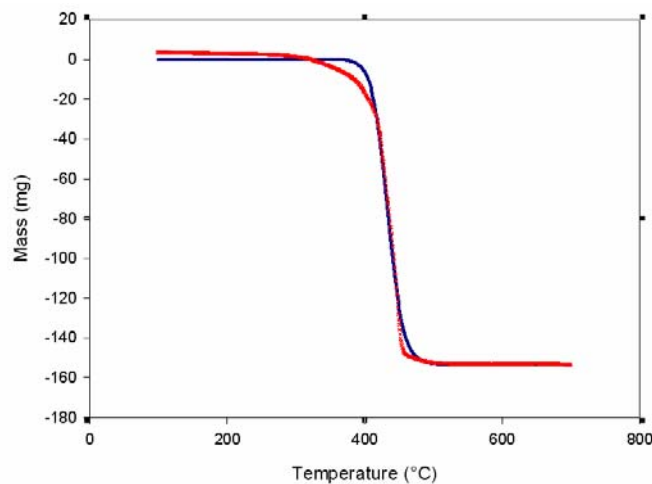
Figure 4. Removal of Ancormax D from a Fe-C compact at 10°C/min.
Comparison between predicted (blue) and actual (red) weight loss profiles.

Once the weight loss curves are collected, the values of the parameters T_{MAX} and *b* are determined by curve fitting methods for every experimental run, with the software SigmaPlot. These values are obtained from non-smoothed data.

2.3.1 Effect of the presence of nickel

A) The potential catalytic effect of nickel

Study of the literature provides extensive evidence about the catalytic activity that nickel has on the cracking of hydrocarbon chains, suggesting that its presence as an alloying element inside P/M components might alter the chemical mechanisms of lubricant pyrolysis. As an example, nickel is a known catalyst of the methanation reaction (formation of CH_4 from carbon monoxide and hydrogen) [16]. Nickel-supported catalysts are also used in order to enhance the conversion of hydrocarbons to CO, CO_2 and methane [17], in the range of 20°C to 550°C. As far as the

pyrolysis of EBS is concerned, studies recently proved that the iron / graphite matrix had a strong catalytic effect on the conversion of EBS to gas phase products [18]. Similarly, nickel could potentially promote the same reaction since the pyrolysis of EBS is known to be metal-mediated [19].

B) <u>TGA results</u>

Figures 5 & 6 show the evolution of T_{MAX} with increasing heating rates, for the three alloy systems used and for both lubricants. T_{MAX} appears to increase almost linearly with heating, whereas no noticeable effect due to the presence of nickel is observed. This is supported by the narrowness of the error bars.
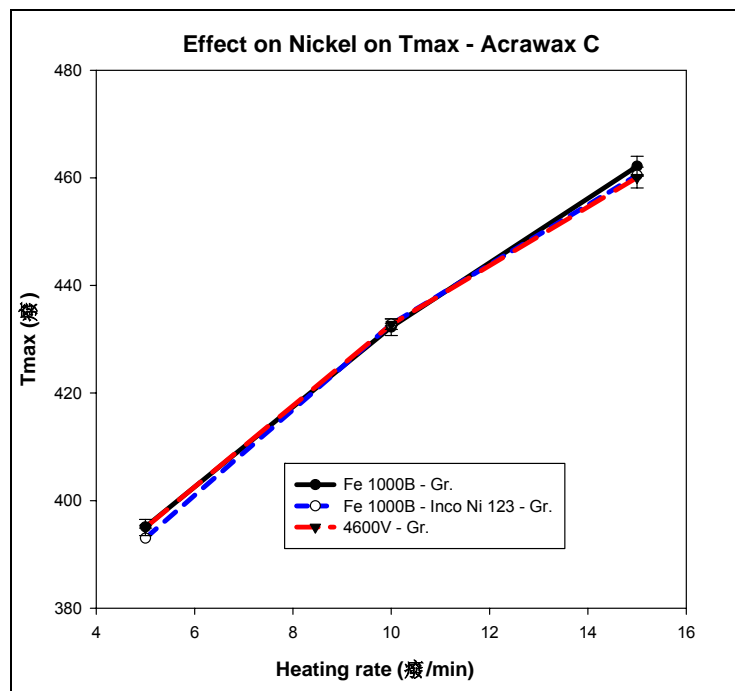
Figure 5. Effect of nickel and heating rate on T_{MAX} (Acrawax C).
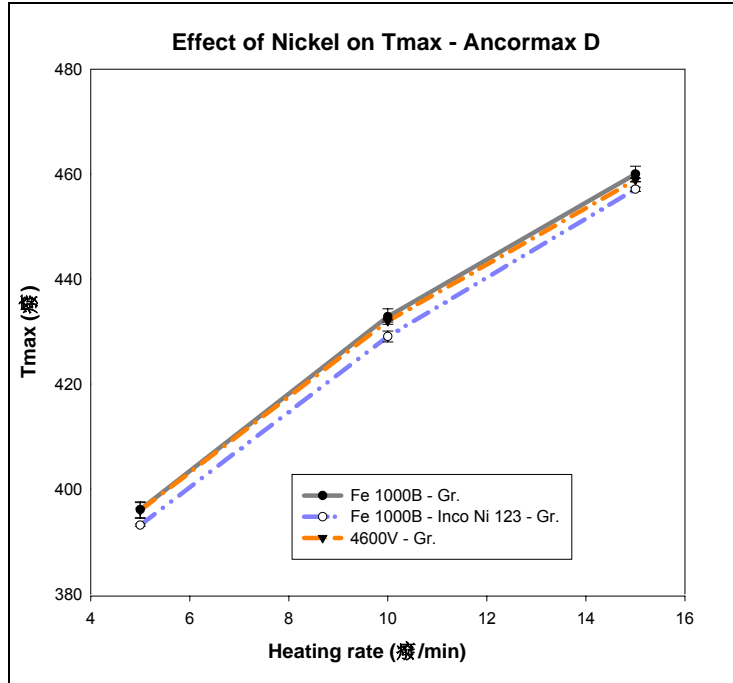
Figure 6. Effect of nickel and heating rate on T_{MAX} (Ancormax D)

Figures 7 & 8 show the corresponding values of the parameter b, under the same experimental conditions. The overall trend is an increase in the value of b as the heating rate increases, which is consistent with previous works on delubrication [7, 10]: as the green compacts are heated faster, the lubricant is removed over a narrower range of temperatures. Here, an effect of Nickel can be observed: for a given heating rate, Nickel-containing samples lose mass (attributed to lubricant removal) at a slightly slower rate; this phenomenon is more pronounced in the case of green compacts containing admixed Nickel. As pointed out earlier about nickel's potential role as a catalyst, it can be suggested that for a given surface area of contact between the lubricant particles and the metal/graphite matrix, the presence of nickel would somewhat promote the conversion of lubricant decomposition by-products to smaller molecules, thus requiring a bit more time for these gaseous species to escape from the compact.

11
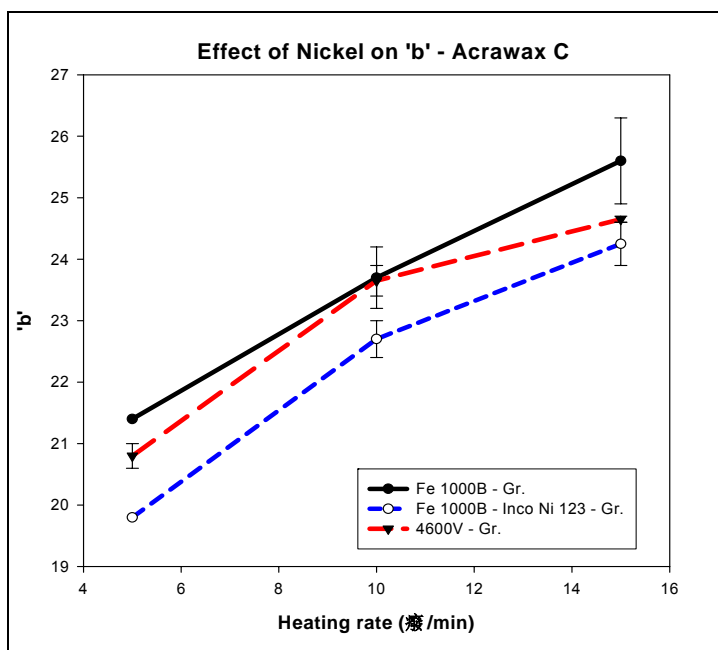
Figure 7. Effect of nickel and heating rate on 'b' (Acrawax C).
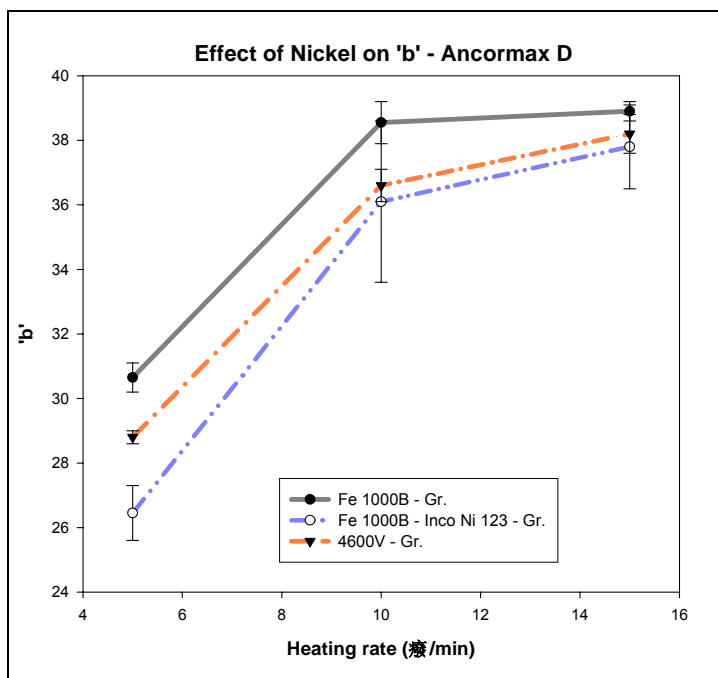
Figure 8. Effect of nickel and heating rate on 'b' (Ancormax D).

A) Statistical analysis

A statistical analysis of variance is performed in order to evaluate the relative contributions of the heating rate and the presence of Nickel on the parameters T_{MAX} and b. Also, the possible existence of an interaction between the heating rate and the presence of nickel is investigated. The data passes the normality test, and the Q-Q plots fits very closely a straight line, which means that the observed variations of T_{MAX} and b are almost completely explained by changes in the heating rate or alloy composition. This analysis is also based on the assumption that the order in which the experimental runs were performed has no effect on data collection.

Results show clearly that, for the removal of both Acrawax C and Ancormax D, the heating rate is the dominating factor (88% contribution for Acrawax C, 90% contribution for Ancormax D). The residual value of variance for the contribution of nickel to variations in T_{MAX} does not even exceed the minimal threshold value for significance. This means that, from a statistical point of view, T_{MAX} is affected in no way by the presence of nickel, and supports the hypothesis: even if the alloying nickel enhanced the decomposition of lubricant molecules into smaller compounds, it would affect the thermodynamics of lubricant evaporation.

Regarding the impact of the presence of nickel to the response of b, the analysis of variance performed in this study shows that contributions of 9% and 5% are observed, respectively for the removal of Acrawax C and Ancormax D (*Table 3).*

Lastly, the analysis shows that there exists no interaction between the heating rate and the presence of alloying nickel, in terms of contribution to the values of T_{MAX} and b.

% Contribution	Acrawax C	Ancormax D
Heating rate	88%	90%
Presence of Nickel	9%	5%
Error factor	3%	5%

Table 3. Contributions of the presence of nickel / heating rate on the kinetics of delubrication. (variations in the response of the parameter b).

2.3.2 Effect of green density

Figures 9 & 10 show the effect that green density has on the kinetics of lubricant removal. Previous works on the contribution of this parameter concluded that increasing green densities would make it harder for the lubricant to escape the parts [12]. However, the present results tend to prove that in fact, for compacts pressed to green densities below 94% of the theoretical full density, no noticeable impact is observed on the kinetics of lubricant removal.
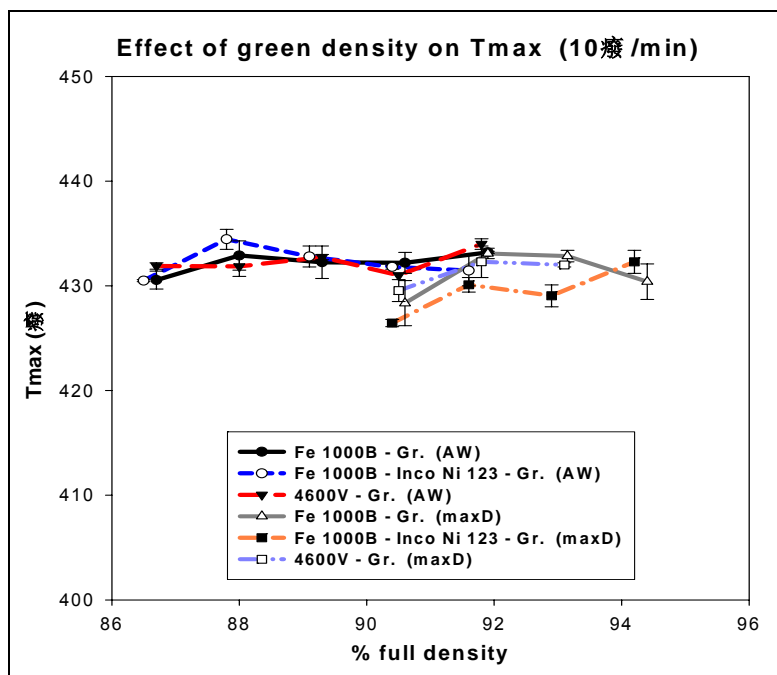
Figure 9. Effect of green density on T_{MAX} (Acrawax C, Ancormax D).
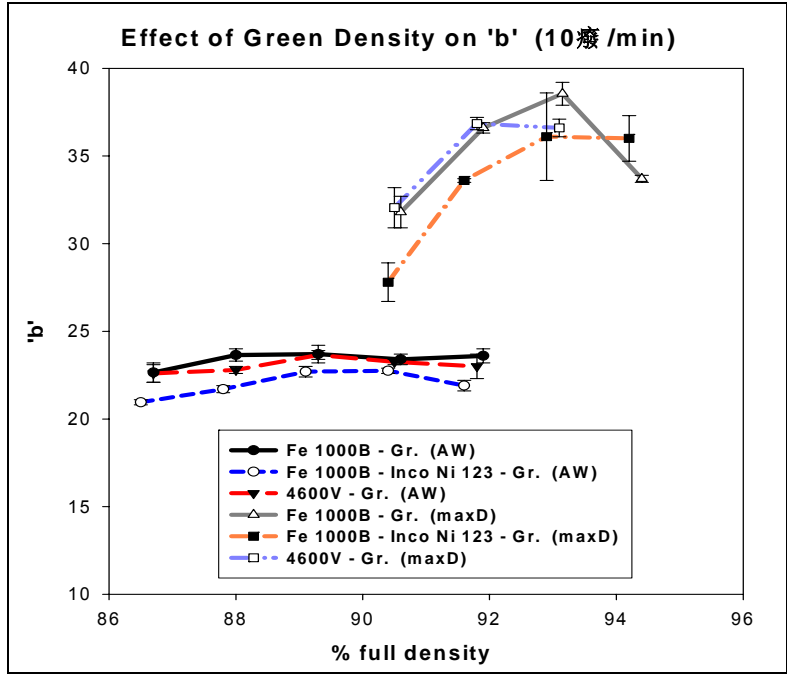
Figure 10. Effect of green density on 'b' (Acrawax C, Ancormax D).

For both cold-compacted parts (Acrawax C) and warm-compacted parts (Ancormax D), the fluctuations of T_{MAX} for varying green densities remain below ca. 5°C over the range of densities used. For the case of Acrawax C delubrication, the parameter b is not affected by green density, while for Ancormax D delubrication occurs over a narrower range of temperature (increase in the value of b) as the green density increases. This effect is rather pronounced, as the average value of b goes, for instance in the case of the compacts containing admixed nickel, from 27.8 to 36 as the green density increases from 90.5 to 94.3% full density. This phenomenon might be related to the procedure of warm compaction, and an explanation can be proposed, if we assume that the decomposition behaviour of Ancormax D is similar to that of Acrawax C. Indeed, it has been shown that the iron/graphite matrix in which the lubricant is dispersed has a catalytic effect on the formation of gas phase products, upon heating of the compacts [18]. If we assume that the conversion of Ancormax D to small hydrocarbons is also enhanced by the iron/graphite matrix, then warm compaction of the iron/graphite/lubricant powder to higher densities will activate this

15

catalytic phenomenon, by simply increasing the surface area of contact between the particles of Ancormax D and the particles of iron and graphite. As a result of this, once the heat provided by the furnace is sufficient to allow evaporation of Ancormax D and its decomposition by-products (i.e. at temperatures approaching T_{MAX}), a process of enhanced lubricant decomposition, combined with hydraulic pressure coming from the melted, undecomposed lubricant [20], will lead eventually to a faster release of delubrication by-products out of the compacts (i.e. increase in the value of b). Not only would a higher green density (for warm compaction) potentially lead to an increased contact surface area between lubricant and metal particles, but it would also lead to a lack of available open porosity, at the origin of the hydraulic pressure mentioned above

This explanation is partly supported by the fact that McGraw and al. [20] observed a faster lubricant removal at higher densities, for both bronze and iron powders. However, their measurements were not dynamic, and instead the samples were weighted at temperature interval of 55°C.

2.3.3 Effect of compact geometry

A) <u>Need for a correction factor</u>

The indicator used in the present work as a characteristic of compact geometry is the ratio surface/volume, which is related to the average distance over which the gaseous by-products of lubricant decomposition have to travel before they reach the compact surface. However, this value does not take into consideration the fact that considerably more open porosity is available for lubricant removal on the top and bottom faces of the compacts, than on the lateral faces [12]. This discrepancy tends to be even more pronounced at higher green densities, as the metal particles present on the compact lateral faces undergo additional plastic deformation during die ejection, thus closing their adjacent pores.

For this reason, a correction factor was defined in order to take into consideration the non-uniform distribution of open porosity, over the entire surface of the compacts. Indeed, it is really the overall surface area of open pores which dictates the mechanism of diffusion / convection of

gaseous species out of the green compacts. This correction factor, Ω, allows the use of an open-porosity corrected surface / volume ratio. Ω is defined as:

$$\Omega = [amount\ of\ open\ porosity]_{TOP} / [amount\ of\ open\ porosity]_{SIDE.}$$

Thus, stereomicroscopic pictures of the green compacts (Fe 1000B/Graphite/Acrawax C, density $6.95g.cm^{-3}$) are taken, for both the top and lateral surfaces. The pictures are then digitally post-processed to reconstruct the open porosity of each side: black areas corresponding to the open pores and white areas corresponding to the rest of the compact surface (*Figures 11 & 12*). Finally, the ratio Ω is evaluated to be 3.84 for a $6.95g.cm^{-3}$ green density.
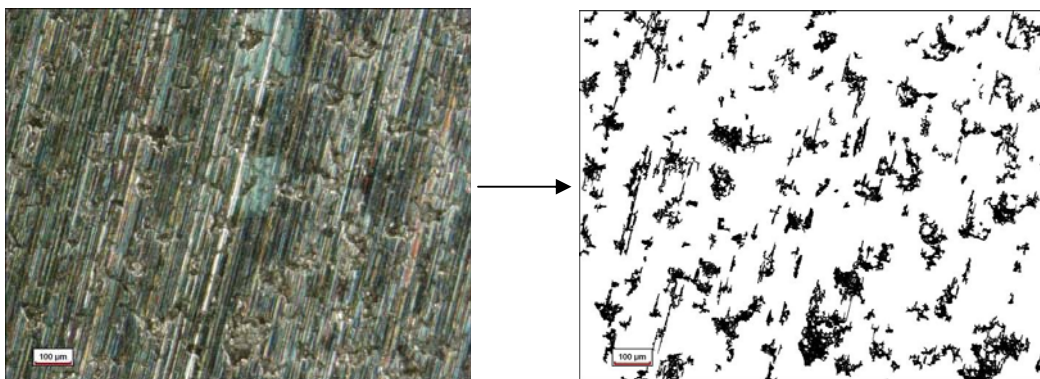
Figure 11. Fe 1000B/Graphite/Acrawax C, $6.95g.cm^{-3}$, side surface. Scale bar: 100 µm.
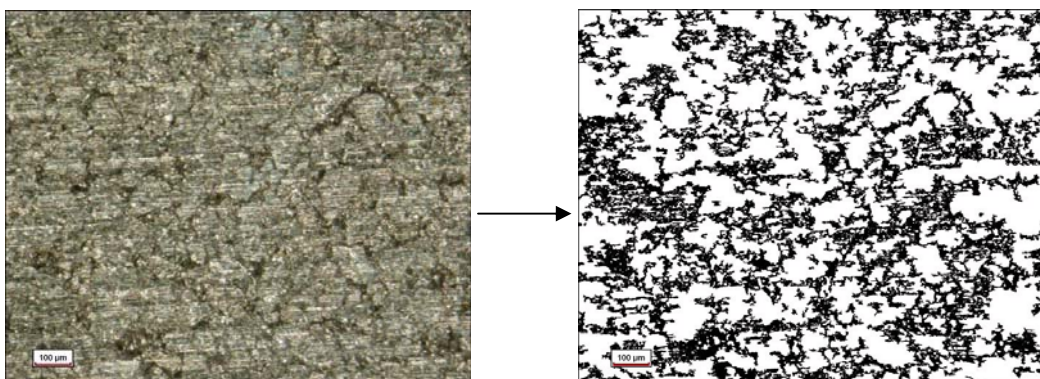
Figure 12. Fe 1000B/Graphite/Acrawax C, $6.95g.cm^{-3}$, top surface. Scale bar: 100 µm.

In other terms, the samples used in this study exhibit almost four times more open porosity on their top and bottom surfaces than on their lateral surfaces, when pressed to a green density of 6.95g.cm^{-3}. Since the stereomicroscopic study is only carried out on the top and lateral surfaces of the compacts, the method is detailed here is only valid if we assume that:

$$[amount\ of\ open\ porosity]_{BOTTOM}\ /\ [amount\ of\ open\ porosity]_{SIDE}$$
$$=\ [amount\ of\ open\ porosity]_{TOP}\ /\ [amount\ of\ open\ porosity]_{SIDE}.$$

Calculation of the open porosity-corrected surface / volume ratio is made by assigning the factor 0.51*Ω to the surface area of the top and bottom surfaces of the compacts, and a factor 0.51 to the lateral surfaces. The reason for the use of an additional coefficient 0.51 is that, for this given distribution of open porosity, the corrected surface / volume ratio of a cube would remain unchanged. For the rectangular and cylindrical compacts used in the present work, the corrected surface / volume ratios are respectively 0.439mm^{-1} and 0.572mm^{-1}.

B) <u>Data analysis</u>

Figures 13 & 14 show, for both geometries, the evolution of T_{MAX} and b with increasing heating rates (from 5°C/min to 15°C/min). For the present set of TGA measurements, a metallic sample holder was utilized, as the cylindrical compacts did not fit into the ceramic crucible. The induced change in the temperature field around the samples explains the shift in the values of T_{MAX}, in the case of rectangular compacts delubrication. However, the characteristic pseudo-linear increase of T_{MAX} with respect to the heating rate, observed in the preceding section, is still observed here.

18
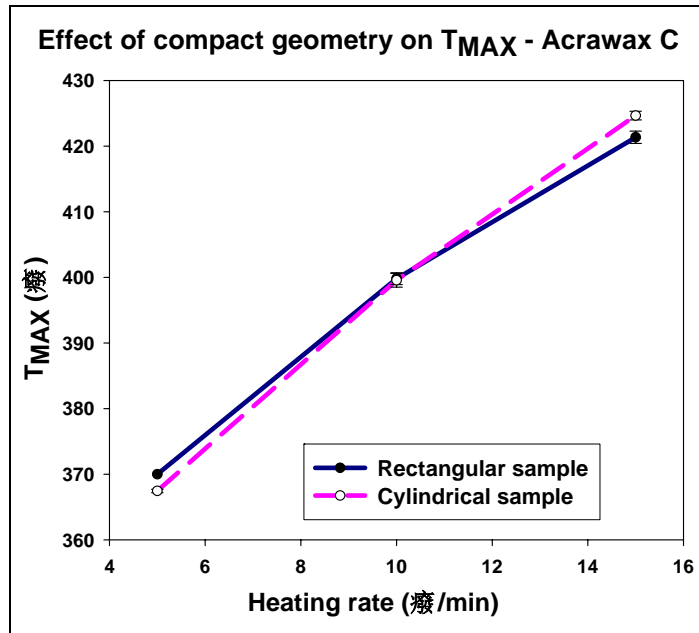
Figure 13. Evolution of T_{MAX} with increasing heating rates. Rectangular & cylindrical samples. Green density = 6.95g.cm^{-3}.
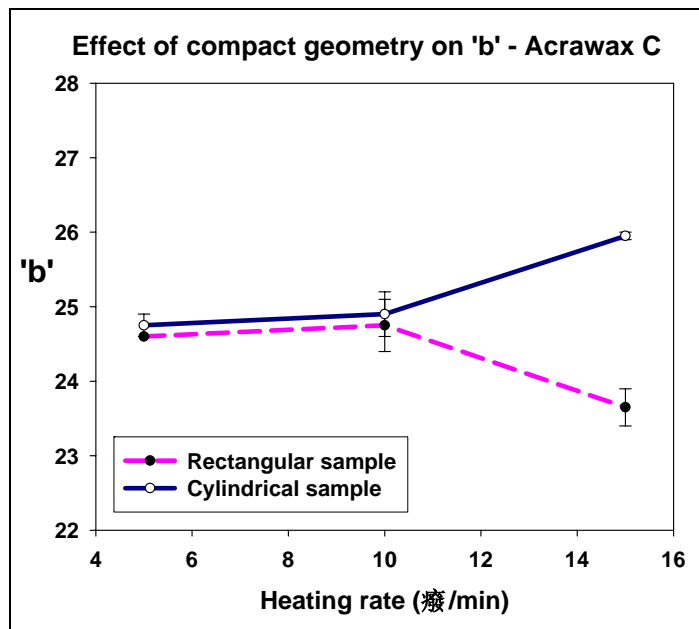
Figure 14. Evolution of 'b' with increasing heating rates. Rectangular & cylindrical samples. Green density = 6.95g.cm^{-3}.

The main outcome of these measurements is that the values of T_{MAX} for the two geometries are extremely close. At low heating rates (5°C/min), 50% lubricant removal occurs at a slightly lower temperature (less thank 5°C difference) for cylindrical samples, whereas at higher heating rates (15°C/min), 50% lubricant removal is achieved faster in the case of rectangular samples (less than 5°C difference in this case too). *Figure 15* proves that, for the intermediate value of the heating rate, the weight loss profiles for both geometries completely overlap. If an increase in the amount of available open porosity was to have any impact of the kinetics of delubrication, the 30% difference between the corrected S/V ratios of our samples would be enough to observe, on *Figure 13*, a noticeable deviation in the values of T_{MAX} from one curve to the other.

The present data seem to be in contradiction with the results of previous studies, which reported that faster lubricant removal occurred with increasing surface/volume ratios [20, 21]. Nevertheless, these studies were performed using samples of various volumes, hence various masses. For that matter, it is not possible to attribute the change in delubrication kinetics only to the varying geometry of the samples. Obviously, completion of the delubrication process should be delayed if the size of a P/M component is augmented while the geometry is kept identical. This aspect of the problem was disregarded by the mentioned studies.
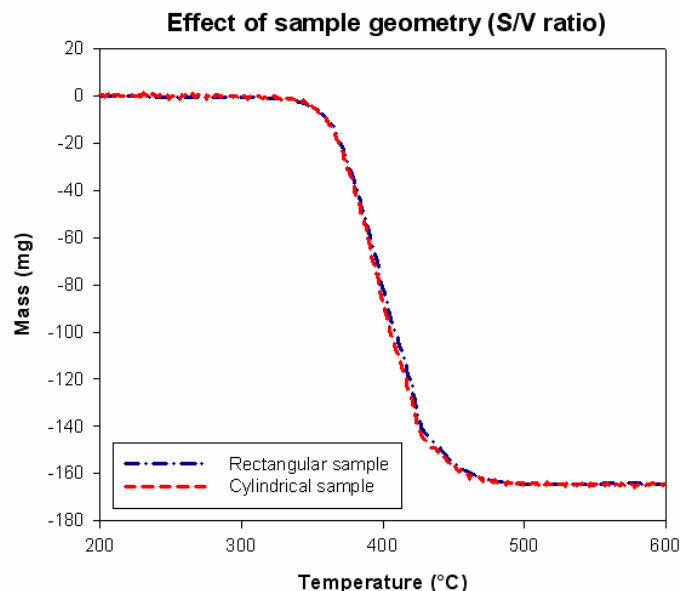
Figure 15. Effect of sample geometry on the weight loss profile. Heating rate: 10°C/min. Green density = 6.95g.cm^{-3}.

These results do not completely agree with those obtained by McGraw and al. [20]. Their observations for iron-based powders show that delubrication tends to be faster for higher values of the S/V ratio. Yet, the method they use is questionable regarding the interpretation of the weight loss profiles: samples are heated at 150°C/min during four minutes, and then weighted.

We do not have at this point an explanation for the behaviour of the response of the parameter b: comparable values of b are obtained at lower heating rates, while they start diverging as the heating rate increases from 10°C/min to 15°C/min. Nevertheless, the value of b remains high enough, under any processing conditions, so that it is safe to suggest that the time of complete lubricant removal will almost not be affected.

What can be drawn from these experiments is that, for compact weights below ca. 30g, the geometry of the part has no effect on the kinetics of lubricant removal. The extra open porosity available in the case of the cylindrical samples (+30%) does not make delubrication faster. This implies that the step of lubricant decomposition / evaporation would the kinetically limiting factor.

2.4 Conclusions

The present study investigated the respective effects of green density, compact geometry and presence of nickel on the kinetics of lubricant removal. It appears that nickel has very little effect on the time of complete delubrication, even though the range of temperatures over which weight loss takes place is somewhat narrowed down by the presence of alloying nickel. The fact that neither green density nor compact geometry has an impact on the kinetics of the process proves that the kinetically limiting factor is the combined process of lubricant decomposition + evaporation. Lastly, it was possible to explain the observed dependencies of T_{MAX} and b by suggesting that T_{MAX} relates to an overall evaporation temperature, while b is representative of breakdown kinetics of lubricant molecules.

2.5 References

[1] German, R.M., *Powder Metallurgy Science*. 1984, Princeton, N.J.: Metal Powder Industries Federation. viii, 279.

[2] German, R.M., *Powder Metallurgy & Particulate Materials Processing*. 2005, Princeton, N.J.: Metal Powder Industries Federation. 528.

[3] Legzdins, C.F., I.V. Samarasekera, and T. Troczynski, *A comparative study of delubrication and associated defects for high temperature sintered ferrous materials.* Advances in Powder Metallurgy and Particulate Materials, 1999. **1**: p. 3-57-3-72.

[4] Legzdins, C.F., I.V. Samarasekera, and T. Troczynski. Experimental studies of Zinc stearate delubrication in high temperature sintering of ferrous compacts. in PM Tech. 1999. Vancouver, BC.

[5] Takata, Z., H. Takigawa, and N. Kawai, *Behavior of dimensional change in sintering of Fe-based powders.* KOBELCO Technology Review, 1990(9): p. 5-9.

[6] Samal, P.K., *Factors affecting corrosion resistance of powder metal (P/M) stainless steels.* Key Engineering Materials. 2nd International Latin-American Conference on Powder Technology, 2001. **189-191**: p. 328-339.

[7] Saha, D. Delubrication during sintering of P/M compacts: Operative mechanism and process control strategy, in Materials Science and Engineering. 2001, Worcester Polytechnic Institute: Worcester, MA. p. 120.

[8] Saha, D. and D. Apelian. Optimization of delubrication during sintering. in International Conference on Powder Metallurgy & Particulate Materials. 2000. New York, NY, USA.

[9] Saha, D. and D. Apelian. Control of de-lubrication utilizing a logistic function based empirical model. in Advances in Powder Metallurgy and Particulate Materials - 2001, May 13-17 2001. 2001. New Orleans, LA, United States: Metal Powder Industries Federation.

[10]Saha, D. and D. Apelian, *Control strategy for de-lubrication of P/M compacts.* International Journal of Powder Metallurgy (Princeton, New Jersey), 2002. **38**(3): p. 71-79.

[11]Nayar, H.S. Delubrication problems & solutions in the P/M industry. in Proceedings of the 1994 International Conference & Exhibition on Powder Metallurgy & Particulate Materials. Part 3 (of 7), May 8-11 1994. 1994. Toronto, Can: Metal Powder Industries Federation, Princeton, NJ, USA.

[12]Auborn, J.N. and J.S. Choo. Effect of chemistry and compact density on the decomposition of P/M lubricants. in Proceedings of the 1994 International Conference & Exhibition on Powder Metallurgy & Particulate Materials. Part 3 (of 7), May 8-11 1994. 1994. Toronto, Can: Metal Powder Industries Federation, Princeton, NJ, USA.

[13]Hoeganaes, Data sheet: Ancorsteel 4600V.

[14]Hoeganaes, Data sheet: Ancorsteel 100, 1000B, 1000C.

[15]Rutz, H.G. and F.G. Hanejko, High density processing of high performance ferrous materials by new P/M process. Industrial Heating, 1994. **61**(12): p. 39-43.

[16]Nakano, H., et al., *Carbon deposition by disproportionation of CO on a Ni(977) surface.* Surface Science, 2000. **Vol. 454-456**: p. pp. 295-299.

[17]Sutton, D., et al., Investigation of nickel supported catalysts for the upgrading of brown peat derived gasification products. Bioresource Technology, 2001. **80**(2): p. 111-116.

[18]Poskrebyshev, G.A., et al. Mechanism of N,N'-ethylenebisstearamide pyrolysis and formation of CO, CO2, CH4 and C2H4 of in the presence of iron/carbon powder under

vacuum at 300C < T < 700C. in 229th American Chemical Society National Meeting & Exposition. 2005. San Diego, CA.

[19]Baum, M.M., et al., *Lubricant pyrolysis during sintering of powder metallurgy compacts.* Metallurgical and Materials Transactions B: Process Metallurgy and Materials Processing Science, 2004. **35**(2): p. 381-392.

[20]McGraw, J., M.J. Koczak, and A. Kao, *Investigation in the Delubrication of P/M Compacts.* International Journal of Powder Metallurgy (Princeton, New Jersey), 1978. **14**(4): p. pp. 277-280, 283-285, 287-288.

[21]Oliveira, R.V.B., et al., Ceramic injection moulding: Influence of specimen dimensions and temperature on solvent debinding kinetics. Journal of Materials Processing Technology, 2005. **160**(2): p. 213-220.

3.0 Chemical Mechanisms of Delubrication

3.1 Introduction

Manufacturing of components in the powder metallurgy industry requires that lubricants are admixed to the metal particles by 1% weight. A sharp decrease in the ejection forces during parts ejection from the die accompanied by an extension of die life are the main two benefits resulting from lubrication. Besides, handling of the 'green' compacts is made easier, and the parts breakage rate tends to be reduced [1, 2].

Yet, this need for lubrication induces a need for delubrication, as most of the lubricant mass remains inside of the compacts while they enter the sintering furnace. Therefore, the entering zone of furnaces is usually dedicated to the thermal removal of lubricant, by means of a steady, though mild heating of the parts from 300°C up to 900°C. The sequence of events was initially identified as such: melting of the lubricant, decomposition of its chemical constituents into smaller molecules, followed by the evaporation and the diffusion of these compounds through an interconnected network of pores [3]. As a final step, the gaseous species reaching the surface of the green compacts are swept away by the gases flowing through the sintering furnace.

If performed improperly, this step of P/M processing can be deleterious to the quality of the end products. More specifically, dimensional changes can be observed after poor control of the delubrication process [4]. The same goes for the corrosion resistance of P/M stainless steels, partially dictated by the efficiency of lubricant removal [5]. Other common delubrication-related defects include, but are not limited to, formation of cracks inside the compacts and carbon deposition, potentially leading to localized carburization/melting of the alloy [6, 7].

While the kinetic aspects of delubrication are better highlighted by means of thermogravimetric experiments, the dual comprehensive study of the reaction mechanisms involved during lubricant decomposition have regularly been addressed by resorting to Fourier Transformed Infrared (FTIR) and Gas Chromatography / Mass Spectrometry measurements. Several studies on delubrication have focused on the analysis of EBS (ethylene bisstearamide)

decomposition by-products. EBS (chemical structure shown in *Figure 16*) is the main constituent of Acrawax C, a lubricant widely used in the P/M industry.
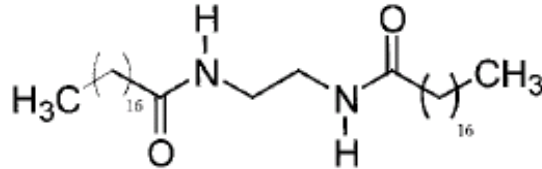
Figure 16. Chemical structure of the EBS molecule.

Thus, White and Nayar [8] showed the presence of N-H, $-CH_2$ and $-CH_3$ functional groups in the furnace atmosphere, as well as they demonstrated the existence of CO, CO_2 and C_2H_4. Nevertheless, heating of the compacts was then only performed up to 600°C.

Efforts were made more recently to understand the mechanisms of lubricant decomposition upon heating, and several key features of this process have now been identified [9]. A combination of FTIR and GC/MS measurements established that numerous gaseous species with a strong hydrocarbon absorption band were emitted during heating of the green compacts. The peak emission of these species is especially observed at a temperature that closely matches that of maximum weight loss rate [10], and which can be estimated to be 450°C. Among these hydrocarbons, CH_4 and C_2H_4 turned out to be the main two products of lubricant decomposition, even though long-chain hydrocarbons were detected. The other major by-product of the delubrication process was proved to be CO_2, and species such as CO and ammonia appeared to be minor by-products. Another finding of the same study concluded that the emission profile of carbon monoxide was bi-modal, a first mild peak occurring at the delubrication temperature, whereas a secondary, strong emission was consistently observed at higher temperatures (about 825°C).

In addition, the impact that the delubrication atmosphere can have on the efficiency of lubricant removal has been thoroughly investigated, and in particular the effect of the moisture presence in the delubrication atmosphere received special attention [9-18]. Somewhat contradictory results on the subject seem to find an answer in Hwang's study [15], the findings of

which conclude that if moisture does not affect the kinetics of lubricant removal, carbon deposition on the compacts are less likely to take place when the delubrication atmosphere dew point is relatively high.

In contrast to this, the effect of alloy composition has been left rather unexplored to this point. Yet, recent studies proved that mixing of the lubricant with the Fe/C powder had in itself an unquestionable catalytic effect [19]. Nickel was identified as the alloying element the more likely to act as a catalyst for lubricant decomposition [3]. Also, the hydrolysis of the EBS molecule has been proved to be metal-mediated [9]. Based on such hints, the present study aims at determining whether or not the presence of alloying elements can modify the reaction mechanisms of delubrication. In the same manner, the effect of the heating rate was investigated. The study was conducted by means of online FTIR measurements combined with GC/MS analysis of the condensable by-products of lubricant pyrolysis.

The final purpose of this study is to establish to what extent the gaseous emission profiles would be affected by a change in the processing conditions. Also, it is of critical importance to verify that at least certain chemical species can be observed in the furnace atmosphere regardless of these processing conditions. This knowledge will assist in the development and design of potential gas sensors for online process control.

3.2 Experimental Procedures

3.2.1 Sample Preparation

Compacts were prepared under the form of 32mm*13mm rectangular bars (TRS bars), with a green density of 6.95 g.cm^{-3}. All compacts weight 29.0 grams and contain 0.6% wt Acrawax C.

Three different alloy compositions are used, which are identical to those used in the first phase of the study: a nickel-free alloy and two compositions with the presence of alloying nickel (admixed and prealloyed).

3.2.2 Description of experiments

The experimental setup used during the experiments is shown in *Figure 17*. The atmosphere used for all the experiments is a dry mixture of 5% H_2 in a balance of N_2. The gas mixture is flown from the gas cylinder through a Teflon® PTFE tubing, at a rate of 80 mL.min^{-1} controlled by a mass flow controller, to a quartz reactor tube. The samples are located in the center part of the reactor tube, and repeatability in the placing of the compact relatively to the tip of the thermocouple is made possible by the presence of two inward quartz bulges, against which the samples are positioned at the beginning of each run.

The heating system of the furnace is divided into three zones of equal length, allowing the use of independent temperature profiles for each zone. During the experiments, the outer zones of the furnace are maintained at a constant temperature of 250°C, while the center zone – in the middle of which the sample is located – is heated linearly from 200°C to 850°C. The sample temperature is monitored independently from that of the furnace, by use of a K thermocouple. The tip of the thermocouple is positioned within 10 mm of the sample, due to the presence of a well on the reactor tube. *Table 4* gives the dimensions of the quartz reactor tube and the single-pass glass cell used.

The gases exiting from the reactor tube exhaust are entirely directed, through a 304 stainless steel tube (680mm*5mmØ) to a Fourier Transformed Infrared Spectrometer (Magna-IR 560, Nicolet, Madison, WI). The stainless steel connecting tube is maintained at 200°C

throughout the experiments, by using a wire heater connected to a temperature controller. A single pass glass cell, used with a set of four sapphire windows (thickness 1mm each, the inner windows being exposed to the gas and the outer windows being exposed to the lab atmosphere), is heated uniformly to 200°C in order to prevent condensation on the optics. Spectra are recorded in the range of 5000 to 500 cm^{-1}.

	Inside diameter (mm)	Length (mm)
Quartz reactor tube (narrow part)	3,7	584,2
Quartz reactor tube (wide part)	22,2	704,9
Single pass glass cell (IR chamber)	15,2	495,3

Table 4. Dimensions of the reactor tube and IR glass cell used for the experiments.

Once they exit the glass cell, the gases are directed, through a non-heated 30cm Teflon® PTFE connecting tube, to a liquid nitrogen trap. The volatile species that do not condense in the liquid nitrogen trap are then directed to a fume hood.

The three heating ramps to which the samples are submitted during the experiments are 5, 10 and 15°C/min. For each heating rate, three different types of samples are delubricated: (i) Nickel-free samples, (ii) samples containing admixed Nickel, and (iii) samples containing prealloyed Nickel.
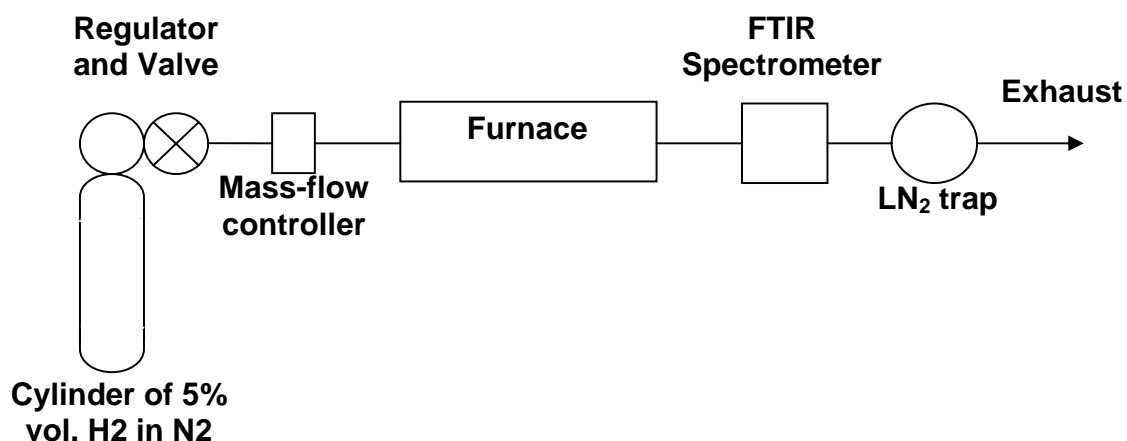
Figure 17. Schematic representation of the experimental setup used in phase II.

3.2.3 Cleaning procedures & observations

The samples, when heated above an approximate temperature of 400°C during an experiment, release a white/yellow particulate product. The presence of this white product, readily condensable, is consistent with the results of previous studies [9]. The reactor tube as well as the connection tubes and the glass cell are precisely maintained at a relatively high temperature in order to hinder condensation of this product.

When condensation occurs inside the quartz reactor tube during an experiment, the tube is then disconnected from the rest of the setup and heated up to 500°C, and subjected to a $2L.min^{-1}$ H_2/N_2 flow, until complete removal of the deposits is achieved. The stainless steel connection tube and the glass cell are also cleaned with acetone between each experiment, and then dried.

Since only the very volatile gases do not condense at the temperature of liquid nitrogen, the more easily condensable by-products of lubricant pyrolysis were trapped in the liquid nitrogen trap, and subsequently dissolved in ca. 5ml of dichloromethane (the uncertainty in the amount of solvent used is estimated to be ± 25%), and stored at a temperature of -8°C, thus limiting any further evaporation of the most volatile species. The glassware used for the LN_2 trap was also cleaned with acetone.

3.3 Signal Processing

3.3.1 Calibration curves

Gas mixtures of known concentrations (methane – 6170 ppm, carbon monoxide – 3002 ppm) are used in order to calibrate the system. Employed in combination with a cylinder of pure nitrogen, mixtures of different concentrations, evenly distributed, were flown at a rate of $2L.min^{-1}$ through the reactor tube and the glass cell – without heating of the furnace. The peak intensities (measured at 2895.036 cm^{-1} for CH_4, at 2176.188 cm^{-1} for carbon monoxide) are plotted as a function of the actual concentration of the mixture being flown.

Figure 18 exhibits a typical infrared spectrum, with strong absorption peaks corresponding to the emissions of hydrocarbons, CO and CO_2. These infrared spectra are post-analyzed with the software OMNIC in order to extract information relative to the intensities of the peaks mentioned above.
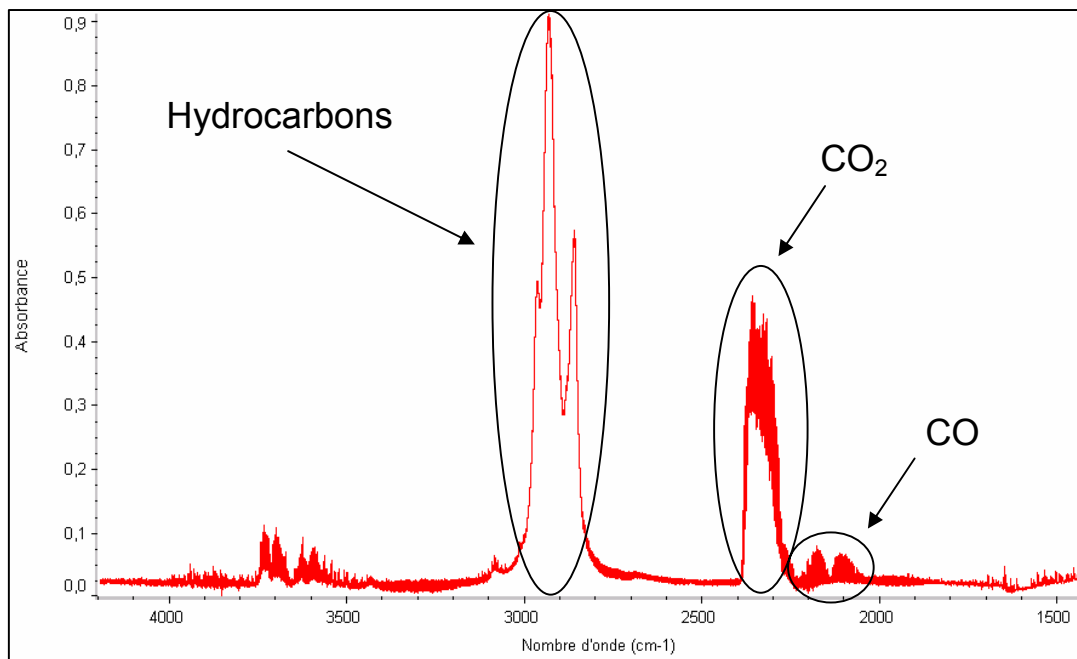
Figure 18. Typical infrared spectrum at delubrication temperature (450°C).
Delubrication of a Fe 1000B/Graphite/Acrawax C compact at 10°C/min.

31

Figures 19 and 20 show the resulting curves. A linear regression is sufficient to fit the calibration curve for CH_4, while a second order regression is required in order to fit the data obtained from CO calibration.

Calibration curve - CH4

$y = 29749x - 133,83$
$R^2 = 0,9971$
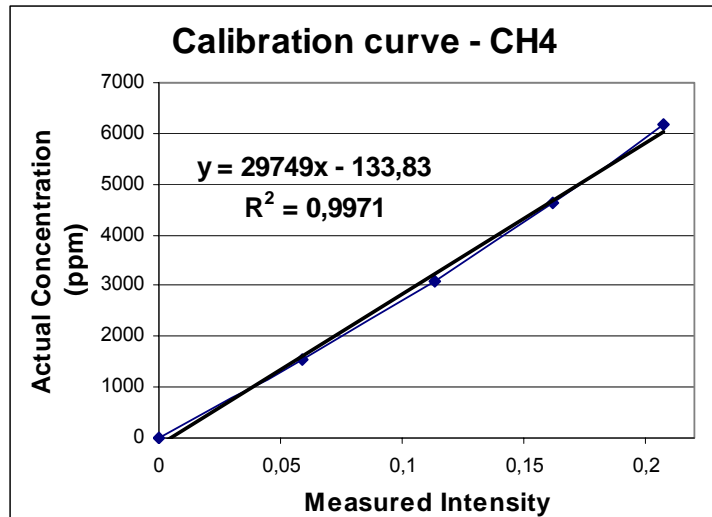
Figure 19. Calibration curve for CH_4.

Calibration curve - CO

$y = 67817x^2 + 1087,8x + 14,74$
$R^2 = 0,9974$
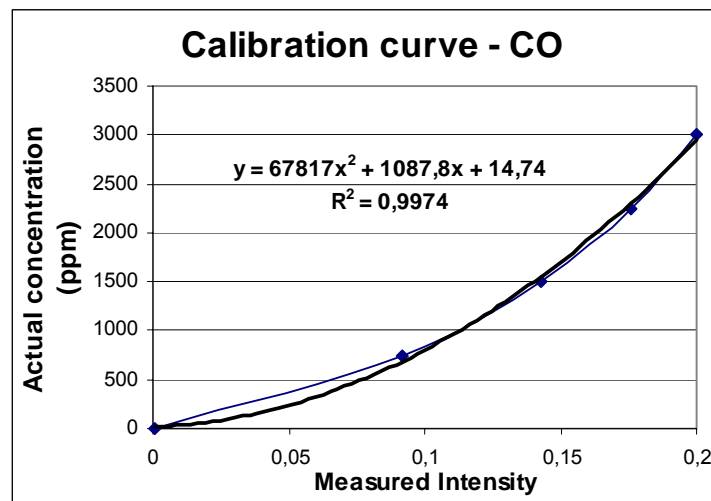
Figure 20. Calibration curve for carbon monoxide.

3.3.2 Correction for convection time

The emission profiles presented in this part of the study were all corrected for convection time. Indeed, there exists a delay during an experiment between the time when the gaseous

species are emitted from the compact, and the time when the same species are detected by the infrared spectrometer.   This time difference was estimated, in terms of corresponding temperature, by calculating the volume of the reactor (from the sample location to the center part of the single pass glass cell), and then dividing this volume by the heating rate used for a given experiment.   These temperature shifts, for heating rates of 5°C/min, 10°C/min and 15°C/min, were respectively 12.5°C, 25°C and 37.5°C.

3.4 Results & Discussion

3.4.1 The potential catalytic activity of nickel

Several works on the catalytic activity of Nickel suggested that in the present study, the presence of Nickel as an alloying element may affect the mechanisms of lubricant pyrolysis. Indeed, Nakano et al. explain that Nickel has a catalytic effect on the methanation reaction (CO + $3H_2 = CH_4 + H_2O$) [20]. If Nickel happened to have a similar effect during the delubrication of P/M compacts, online infrared measurements might then be biased, in terms of the levels of detected CH_4, skewing our estimations towards higher levels of EBS conversion to methane. Park et al. also proved that Fe-Ni bimetallics have a catalytic effect on carbon deposition when respectively exposed to CO/H_2 mixtures, C_2H_4/H_2 mixtures, and $CO/C_2H_4/H_2$ mixtures. However, the relative amount of Ni present in their samples was much greater than the one of the samples used in this study (7:3 for the ratio Ni:Fe). When exposed to the mixtures of CO/H_2 at 600°C, the Fe-Ni bimetallics enhance the conversion of carbon monoxide to carbon filaments, and the process ends when the temperature reaches 725°C [21]. A reverse dependence was found when the catalyst is exposed to a C_2H_4/H_2 mixture. In that case, the same temperature increase has the effect of promoting the conversion of C_2H_4 to methane and ethane and solid carbon [22]. In both situations, there exists a very strong dependence on the Nickel content of the catalyst, in terms of solid carbon yields.

The catalytic effect that Nickel on carbonization reactions was also highlighted in the case of polyimide films [23], even though the reaction then requires presence of an acid. Even Nickel oxides (NiO) can be the precursor to catalysts of the CO hydrogenation reaction. More specifically, NiO treated under a CO/H_2 atmosphere can yield Ni_3C/NiO or $Ni/Ni_3C/NiO$ catalysts [24]. Reciprocally, certain metal oxides were proved to have an impact on the catalytic activity of Nickel. The case study of the deuterium exchange reaction between hydrogen and ammonia showed that the corresponding oxides of the group VIII metals had a significant influence on the catalytic activity of Nickel, even though among this group, Fe oxides turned have to have the less pronounced effect [25]. Other studies in which Nickel was observed to have a catalytic effect on

the conversion of hydrocarbons to CO, CO_2 and methane include the work by Sutton et al. [26], where Nickel-supported catalysts promoted the conversion of brown peat to such volatile species, in the range of 20°C to 550°C.

In the more precise case of pyrolysis of EBS in a solid matrix, recent works proved that the iron / graphite matrix, in presence of which EBS molecules are decomposing, has a strongly pronounced catalytic effect on the conversion to gas phase products [19]. In the same manner, nickel could here again be expected to have a catalytic effect on the breakdown of EBS molecules.

3.4.2 GC/MS measurements

The solid product collected in the LN_2 trap, once dissolved in dichloromethane (procedure explained earlier) was analyzed by GS/MS measurements. *Figure 21* gives an example of the chromatogram obtained during analysis of the white product resulting from the delubrication of a Fe 1000B / Graphite / Inco Ni 123 / Acrawax C sample, at 15°C/min. Each peak of the chromatogram corresponds to a particular chemical compound. Similar chromatograms were generated during the analysis of the other five solutions. *Table 6* summarizes the experimental conditions under which the analyzed products were obtained. The pattern of peak distribution was very similar between all the chromatograms, and the only noticeable differences were in term of the relative yields of each product. *Tables 7a* and *7b* present the data relative to the absolute and relative amounts of each hydrocarbon detected during the GC/MS measurements.

The mass spectra of all the unidentified compounds are reported in appendix A, along with their absolute and relative yields. For all of the compounds which found a match in existing databases, *Table 6* relates the retention time of the detected product to the compound name of the best match. Most of these compounds correspond to alkanes, alkenes, or potentially cycloalkanes. The first two peaks identified with respect to their retention time (i.e. the most volatile compounds), are C_9H_{20} and the corresponding alkene, C_9H_{18}. The largest (thus less volatile) hydrocarbons identified in present work are $C_{16}H_{34}$ and the corresponding alkene, $C_{16}H_{32}$.

The others products listed in *Table 6* (neither alkane nor alkene) were not identified unambiguously by GC/MS measurement, and were selected from a list of possible matches by using the following three criteria:

1. The detected compound exists in the NIST database [30]

2. It can be produced from EBS (contains EBS fragment)

3. It has a reasonably high boiling point (in comparison with hydrocarbons).

Formation of octadecanenitrile and octadecanal are reported for the first time as by-products of EBS pyrolysis. Formation of imidazoline and hexadecanol has been reported previously [9] and is supported by the present work.

General remarks.

The measurements relative to this part of the study were performed on a Shimadzu spectrometer. The delubrication conditions under which the white solid, collected in the LN_2 trap, was produced are summed up in *Table 5*.

Experiment	Alloy composition	Heating rate
A	Fe 1000B – Graphite – Acrawax C	5°C/min
B	Fe 1000B – Graphite – Acrawax C	15°C/min
C	Fe 1000B – Inco Ni 123 – Graphite – Acrawax C	5°C/min
D	Fe 1000B – Inco Ni 123 – Graphite – Acrawax C	15°C/min
E	4600V – Graphite – Acrawax C	5°C/min
F	4600V – Graphite – Acrawax C	15°C/min

Table 5. White solid condensed in the LN_2 trap for GC/MS analysis. Production conditions.

Complete analysis of the collected product was performed for the white solid resulting from experiment D (delubrication of a sample containing 1.85% weight admixed Nickel, heated at 15°C/min). *Table 6* lists, by decreasing retention time inside the GC column, the compounds for which a match was found in existing databases. When values were found in the NIST database, the corresponding molecular weights and boiling temperatures were assigned to each of the identified compounds [29].

It appears that all six chromatograms (experiments A through F) are very similar and, with a few exceptions, contain the same peaks. *Figure 21* represents the chromatogram obtained from analysis of the white product collected during experiment D (Fe-Ni admixed powder, heating rate: 15°C/min).
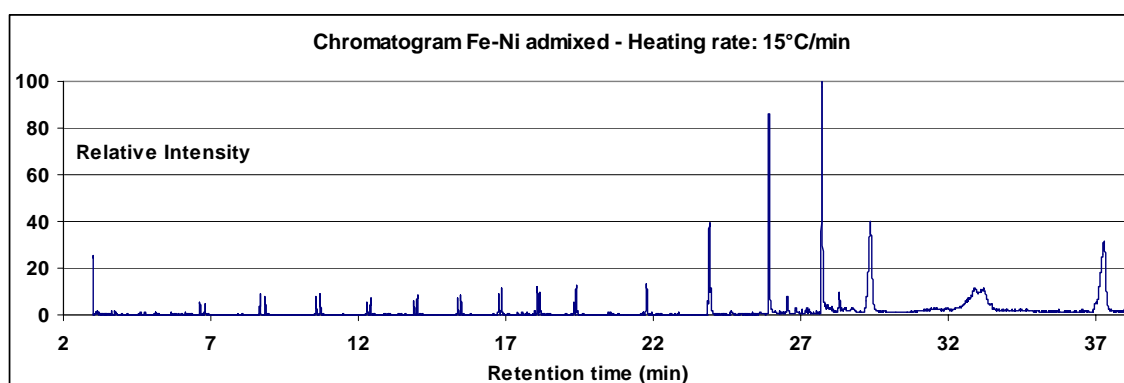
Figure 21. Delubrication of admixed Fe-Ni compact at 15°C/min. White solid chromatogram.

A peculiar feature the data collected by gas chromatography, which has been consistently observed in all the chromatograms, is the presence of unsaturated hydrocarbons pairs of increasing length. Several alkenes/alkanes pairs have thus been identified, even though the formation of cyclohydrocarbons cannot be excluded. The chain lengths for these alkenes/alkanes pairs range from C_9H_{18} and C_9H_{20} to $C_{16}H_{32}$ and $C_{16}H_{34}$, respectively.

Appendix A compiles the chromatograms of all the compounds for which no unambiguous match was found in databases.

Retention time (min)	Base peak (m/z)	T_{BOIL} (°K)	Molecular weight	Best library match	Previously identified
27.8	84	---	338.6	1H-imidazole 2-heptadecyl, 4,5 dihydro-	Yes
23.96	84	---	---	Dodecyl-5methylpirrolidin	No
23.96	84	---	---	Glyodin	No
23.8	58	---	226.40	Pentadecanone	No
23.9	43	---	265.48	octadecanenitrile	Yes
21.93	43	---	268.48	octadecanal	No
21.8	43	---	265.48	octadecanenitrile	Yes
19.45	45	---	242.44	2-Hexadecanol	No
19.39	57	554 ± 10	226.44	Hexadecane	Yes
19.3	43	552 ± 5	224.43	1-Hexadecene	Yes
18.07	41	---	224.43	Hexadecene	No
16.87	57	540 ± 20	212.41	Pentadecane	Yes
16.76	43	541.4	210.40	1-Pentadecene	No
15.47	57	523 ± 10	198.39	Tetradecane	No
15.36	43	524	196.37	1-Tetradecene	No
13.995	57	507 ± 2	184.36	Tridecane	No
13.88	43	504 ± 3	182.35	1-Tridecene	No
12.4	43	489 ± 2	142.28	Dodecane	No
12.29	41	486	168.32	1-Dodecene	No
10.7	43	468 ± 2	156.31	Undecane	No
10.56	41	466 ± 6	154.29	Undecene	No
8.84	43	447	142.28	Decane	No
8.68	55	---	140.25	Cyclooctane 1,2 dimethyl	No
8.68	41	440 ± 10	140.27	1-Decene	No
6.79	43	424	128.26	Nonane	No
6.63	43	419 ± 4	126.24	1-Nonene	No

Table 6. GC/MS data of the white solid collected in the LN_2 trap. Identified compounds. Solid obtained after delubrication of a Fe 1000B/Inco Ni 123/Gr/Acrawax C compact at 15°C/min.

Compound	Ret. Time	A abs.	B abs.	C abs.	D abs.	E abs.	F abs.
1-Nonene	**6.63**	95,509	151,845	131,061	270,728	112,012	354,440
Nonane	**6.79**	187,279	60,634	268,171	151,140	237,799	128,102
1-Decene	**8.68**	50,987	414,132	44,747	416,549	46,194	480,012
Cyclooctane 1,2 dimethyl	**8.68**	50,987	414,132	44,747	416,549	46,194	480,012
Decane	**8.84**	79,705	352,506	73,814	406,258	75,402	386,912
Undecene	**10.56**	138,249	320,368	210,456	422,701	238,510	455,130
Undecane	**10.7**	268,412	261,056	411,852	416,510	460,891	370,706
1-Dodecene	**12.29**	90,467	221,457	149,157	298,161	163,656	409,198
Decane	**12.4**	429,652	52,430	574,984	97,829	609,005	114,623
1-Tridecene	**13.88**	191,317	252,997	303,085	326,703	342,511	466,790
Tridecane	**13.995**	331,342	306,352	550,605	419,046	624,378	567,811
1-Tetradecene	**15.36**	279,459	289,794	470,490	329,961	471,822	439,450
Tetradecane	**15.47**	260,475	443,937	453,517	445,744	568,800	626,253
1-Pentadecene	**16.76**	226,797	547,013	328,199	473,573	420,028	745,628
Pentadecane	**16.87**	16,587	333,543	30,324	201,533	58,358	339,790
Hexadecene	**18.07**	261,522	807,614	446,045	644,815	584,067	976,314
1-Hexadecene	**19.3**	166,180	197,832	284,165	254,805	334,590	317,913
Hexadecane	**19.39**	163,973	792,350	263,462	604,884	475,773	934,875
2-Hexadecanol	**19.45**	14,085	66,959	14,116	62,308	35,216	81,684
octadecanenitrile	**21.8**	20,877	125,422	27,782	124,772	53,932	128,924
octadecanal	**21.93**	18,939	4,128	42,864	56,119	94,789	64,460
octadecanenitrile	**23.9**	950,195	1,415,216	1,379,747	2,103,910	1,822,888	2,138,484
Pentadecanone	**23.8**	35,168	10,544	23,476	5,738	57,417	3,992
Glyodin	**23.96**	250,174	568,302	369,404	377,221	377,102	569,989
Dodecyl-5 methylpirrolidin	**23.96**	250,174	568,302	369,404	377,221	377,102	569,989
1H-imidazole 2-heptadecyl, 4,5 dihydro-	**27.8**	388,612	414,502	374,857	247,408	365,908	334,500

Table 7a. Absolute yields of hydrocarbons from GC/MS measurements (in number of counts). Retention times expressed in minutes.

39

Compound	Ret. Time	A %	B %	C %	D %	E %	F %
1-Nonene	**6.63**	0.92	1.7	1.68	5.09	0.99	4.47
Nonane	**6.79**	1.81	0.68	3.44	2.84	2.11	1.61
1-Decene	**8.68**	0.49	4.64	0.57	7.83	0.41	6.05
Cyclooctane 1,2 dimethyl	**8.68**	0.49	4.64	0.57	7.83	0.41	6.05
Decane	**8.84**	0.77	3.95	0.95	7.64	0.67	4.88
Undecene	**10.56**	1.34	3.59	2.7	7.95	2.11	5.74
Undecane	**10.7**	2.6	2.92	5.29	7.83	4.08	4.67
1-Dodecene	**12.29**	0.88	2.48	1.91	5.6	1.45	5.16
Decane	**12.4**	4.16	0.59	7.38	1.84	5.39	1.44
1-Tridecene	**13.88**	1.85	2.83	3.89	6.14	3.03	5.88
Tridecane	**13.995**	3.21	3.43	7.07	7.88	5.53	7.16
1-Tetradecene	**15.36**	2.7	3.24	6.04	6.2	4.18	5.54
Tetradecane	**15.47**	2.52	4.97	5.82	8.38	5.04	7.89
1-Pentadecene	**16.76**	2.19	6.13	4.21	8.9	3.72	9.4
Pentadecane	**16.87**	0.16	3.73	0.39	3.79	0.52	4.28
Hexadecene	**18.07**	2.53	9.04	5.73	12.12	5.17	12.3
1-Hexadecene	**19.3**	1.61	2.22	3.65	4.79	2.96	4.01
Hexadecane	**19.39**	1.59	8.87	3.38	11.37	4.21	11.78
2-Hexadecanol	**19.45**	0.14	0.75	0.18	1.17	0.31	1.03
octadecanitrile	**21.8**	0.2	1.4	0.36	2.35	0.48	1.62
octadecanal	**21.93**	0.18	0.05	0.55	1.05	0.84	0.81
octadecanenitrile	**23.9**	9.19	15.85	17.71	39.55	16.14	26.95
Pentadecanone	**23.8**	0.34	0.12	0.3	0.11	0.51	0.05
Glyodin	**23.96**	2.42	6.36	4.74	7.09	3.34	7.18
Dodecyl-5methylpirrolidin	**23.96**	2.42	6.36	4.74	7.09	3.34	7.18
1H-imidazole 2-heptadecyl, 4,5 dihydro-	**27.8**	3.76	4.64	4.81	4.65	3.24	4.22

Table 7b. Relative yields of hydrocarbons from GC/MS measurements (% strongest peak).
Retention times expressed in minutes.

<u>Effect of the heating rate on the relative yields of hydrocarbons (based on the GC/MS</u>
<u>measurements of the identified hydrocarbons – *Table 7a*)</u>.

As a general remark, the respective yields of the identified hydrocarbons, resulting from EBS pyrolysis, tend to be promoted with higher heating rates. These yields are multiplied by a factor comprised between 2 and 4 for several compounds (*1-nonene, undecene, 1-dodecene, 1-pentadecene, hexadecene, hexadecane, 2-hexadecanol, octadecanenitrile and glyodin*), when the heating rate used for delubrication is increased from 5°C/min to 15°C/min. In a few cases, the hydrocarbon yields obtained under a 15°C/min heating are even an order of magnitude than those obtained under a 5°C/min (*1-decene, cyclooctane 1,2 dimethyl and pentadecane*).

However, a few by-products of EBS decomposition are produced in smaller amounts when the samples are heated faster (*yields of nonane, decane and pentadecanone respectively divided by 2, 6 and almost 10*).

Finally, the yields of certain species seem to be insensitive to the rate at which the samples are heated (u*ndecane, 1-tridecene, tridecane, 1-tetradecene, tetradecane, 1-hexadecene, octadecanal and imidazole*).

<u>Effect of nickel on the relative yields of hydrocarbons (based on the GC/MS measurements of the</u>
<u>identified hydrocarbons – *Table 7a*)</u>.

 The GC/MS measurements prove that the yields of the same hydrocarbons are also affected by the presence of nickel, though to a much smaller extent. The overall trend is that the production of the hydrocarbons listed in *Table 7a* is promoted by the presence of nickel, and for most of them, the factor by which the yields are multiplied when nickel (either admixed or prealloyed) is present is comprised between 1.5 and 2. This is ratio is high enough to be able to claim that the measured increases in the yields of hydrocarbons cannot only be attributed to measurement uncertainties (±25%). The only compounds of *Table 7a* not to be produced in larger amounts when nickel is present are 1-decene, cyclooctane 1, 2 dimethyl, decane, pentadecane, 2-hexadecanol, glyodin, dodecyl-5methylpirrolidin and imidazole.

It can be observed that pentadecanone is the only compound of *Table 7a* to be produced in smaller amounts when nickel is present in the solid iron/graphite matrix (especially at higher heating rates).

Also, nickel-containing samples tend to be less sensitive to the heating rate, in terms of hydrocarbon yield promotions. Finally, the samples with prealloyed nickel tend to promote the formation of hydrocarbons more than the ones with admixed nickel.

Hypotheses of Ni-modified reaction mechanisms.

A potential indicator for reaction mechanism modification – due to the presence of nickel – would have been the presence of an amine. Indeed, in organic reduction, a nitrile compound can be reduced by reaction with hydrogen in presence of a nickel catalyst. Since octadecanitrile is one of the identified compounds contained in the white solid, an amine could have been formed by the reaction presented here. However, the chromatograms show no unambiguous evidence of amine formation.

Another pathway which could possibly have been activated by the presence of nickel in the iron powder is the metal-mediated reduction of the stearic acid to octadecanol [30], but this assumption is not supported by the data resulting from the GC/MS experiments.

Potential formation of a stearic acid.

A mechanism of lubricant hydrolysis has been proposed in the past [9], leading to a stearic acid ($C_{18}H_{36}O_2$). The hypothesis of stearic acid formation, and its further decarboxylation proceeding by a free radical mechanism, could be supported by the present evidence, as the observed hydrocarbons with less than 17 carbon atoms are potential by-products of this free radical mechanism. *Figure 22* shows the chemical structure of the stearic acid.
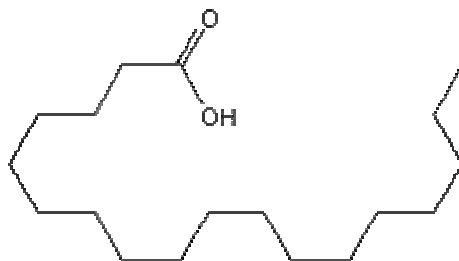
Figure 22. Chemical structure of the stearic acid – $C_{18}H_{36}O_2$.

Possible explanation for the absence of reaction mechanism modification.

A possible explanation for the absence of a Nickel catalytic effect would be that the graphite admixed to the Iron-Nickel would induce a catalyst deactivation. This hypothesis could be supported by the work of Figoli and al. [31].

3.4.3 IR emission profiles

The main by-products of EBS pyrolysis have been measured using Fourier Transformed Infrared (IR) spectroscopy and gas chromatography coupled with mass spectrometry (GC/MS). Time resolved IR spectroscopy has been used to measure *in vivo* product formed during pyrolysis of *EBS*. *Figures 23 through 34* show the temperature dependence of these gaseous emissions: the measured concentrations of hydrocarbons and carbon monoxide are plotted as a function of sample temperature, at the time of emission. According to the infrared spectra collected, the formation of CH_4, C_2H_4, other hydrocarbons, CO and CO_2 is observed, which is supported by the results of previous works [9]. As will be discussed below, several hydrocarbons identified in this study had never been observed in previous studies.
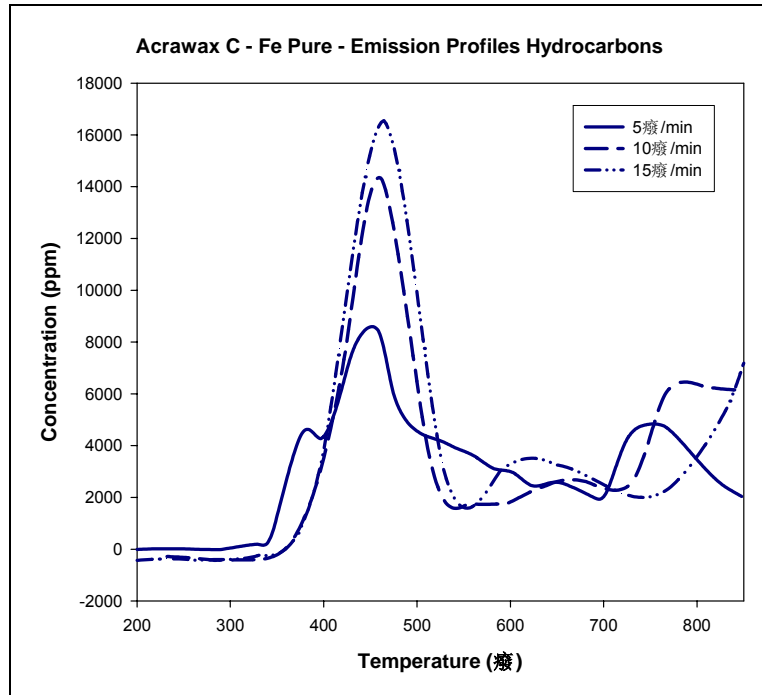
Figure 23. Hydrocarbons IR emission profiles. Fe 1000B/Graphite/Acrawax C samples.
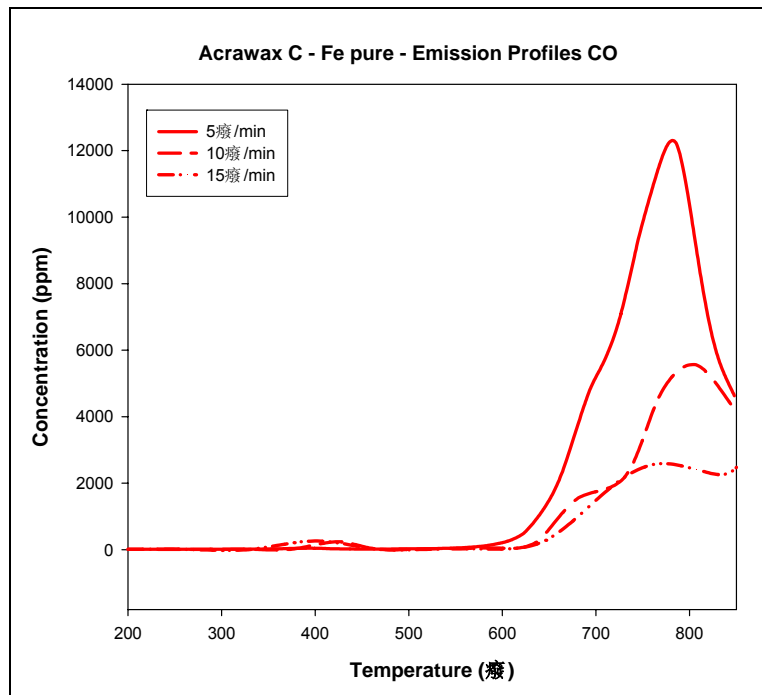
Figure 24. Carbon monoxide IR emission profiles. Fe 1000B/Graphite/Acrawax C samples.
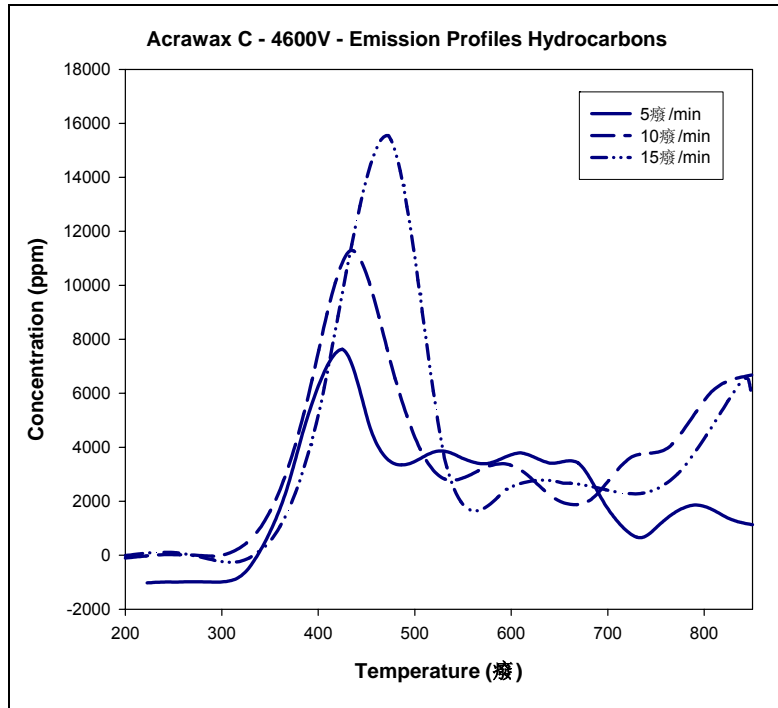
Figure 25. Hydrocarbons IR emission profiles. 4600V/Graphite/Acrawax C samples.
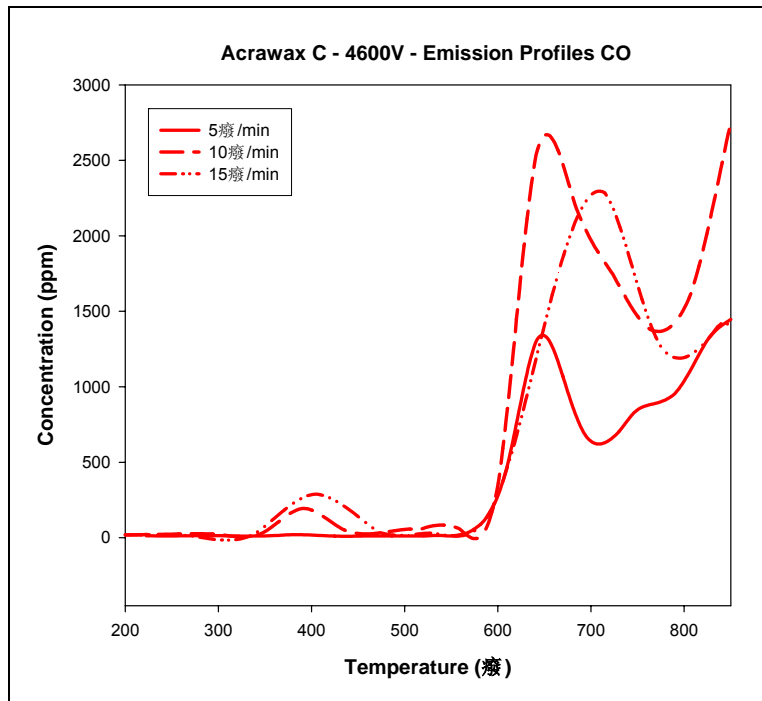
Figure 26. Carbon monoxide IR emission profiles. 4600V/Graphite/Acrawax C samples.
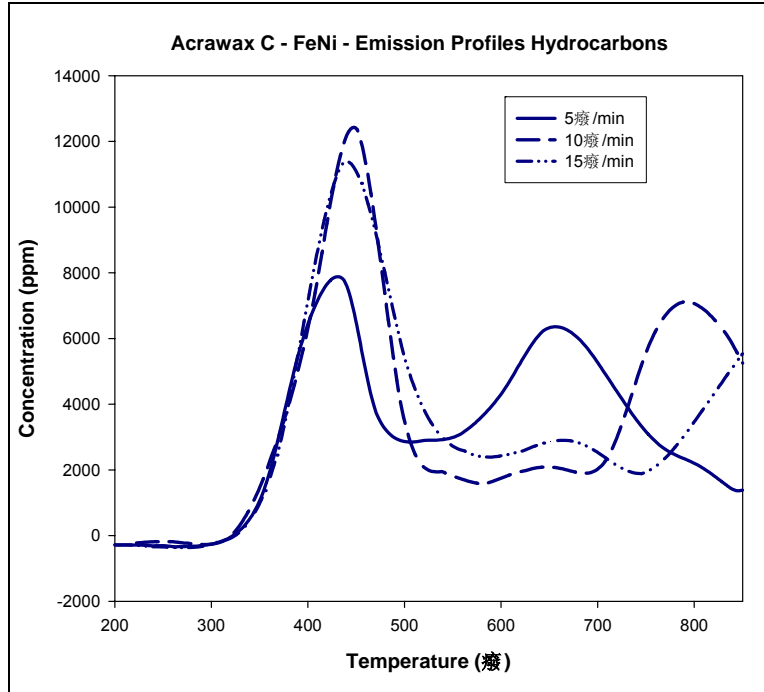
Figure 27. Hydrocarbons IR emission profiles. Fe 1000B/Inco Ni/Gr./Acrawax C samples.
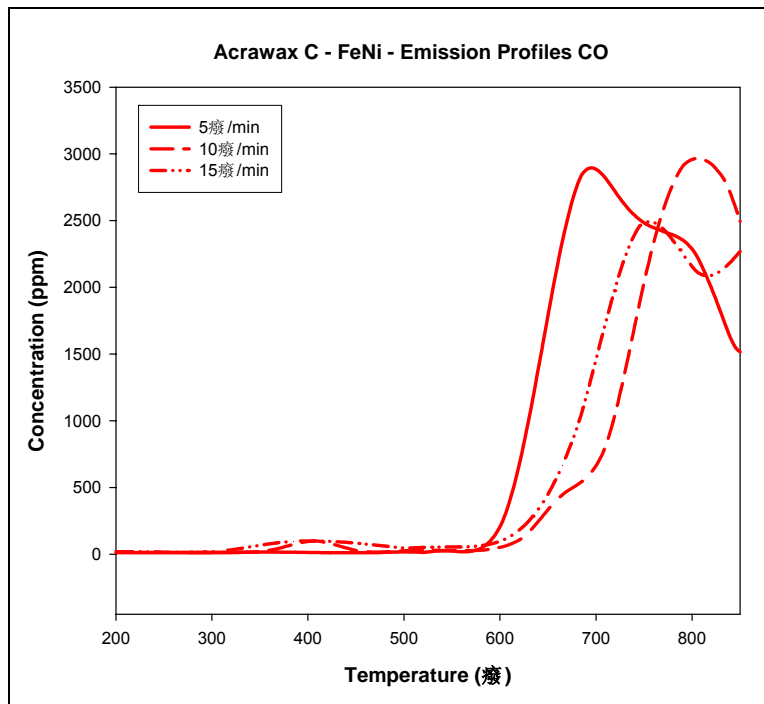
Figure 28. Carbon monoxide IR emission profiles. Fe 1000B/Inco Ni/Gr/Acrawax C samples.
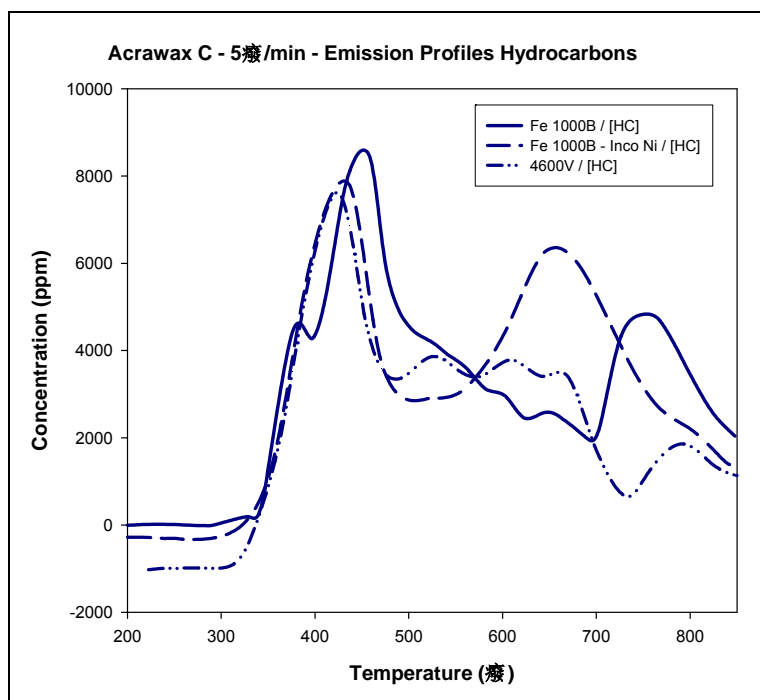
Figure 29. Hydrocarbons IR emission profiles. Acrawax C-lubricated samples [5°C/min].
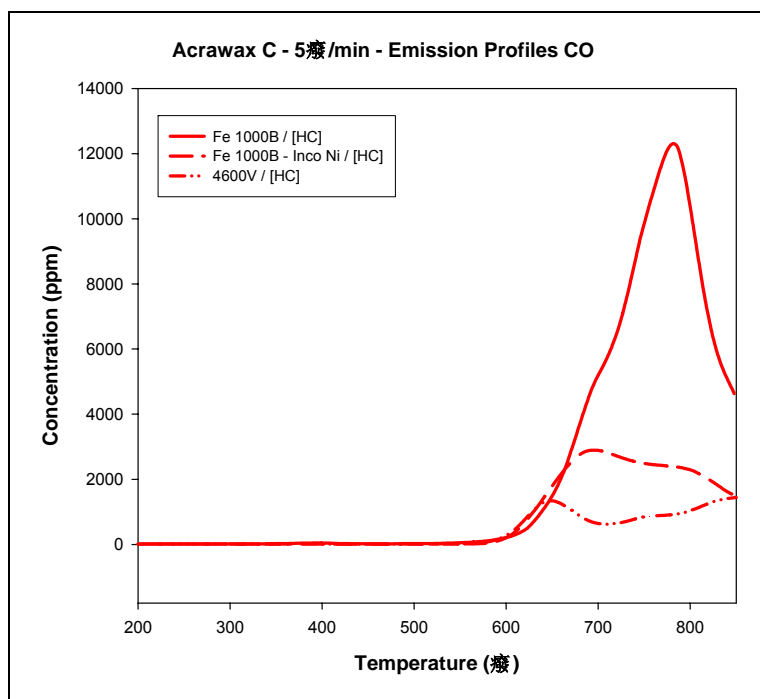
Figure 30. Carbon monoxide IR emission profiles. Acrawax C-lubricated samples [5°C/min].
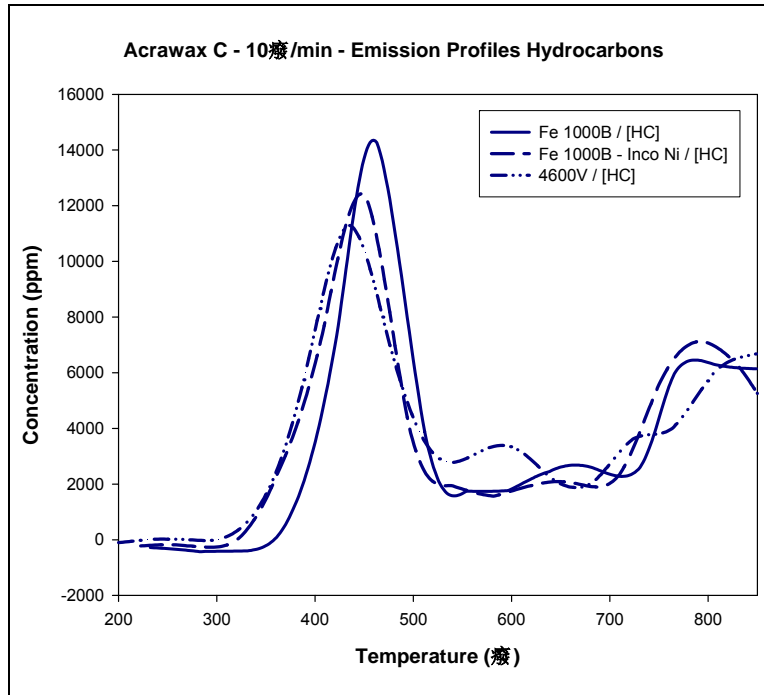
Figure 31. Hydrocarbons IR emission profiles. Acrawax C-lubricated samples [10°C/min].
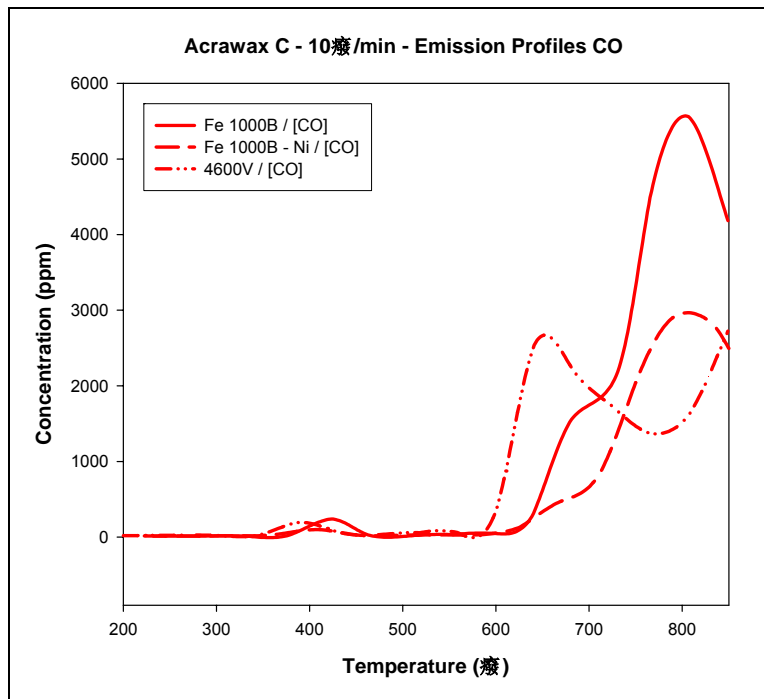
Figure 32. Carbon monoxide IR emission profiles. Acrawax C-lubricated samples [10°C/min].
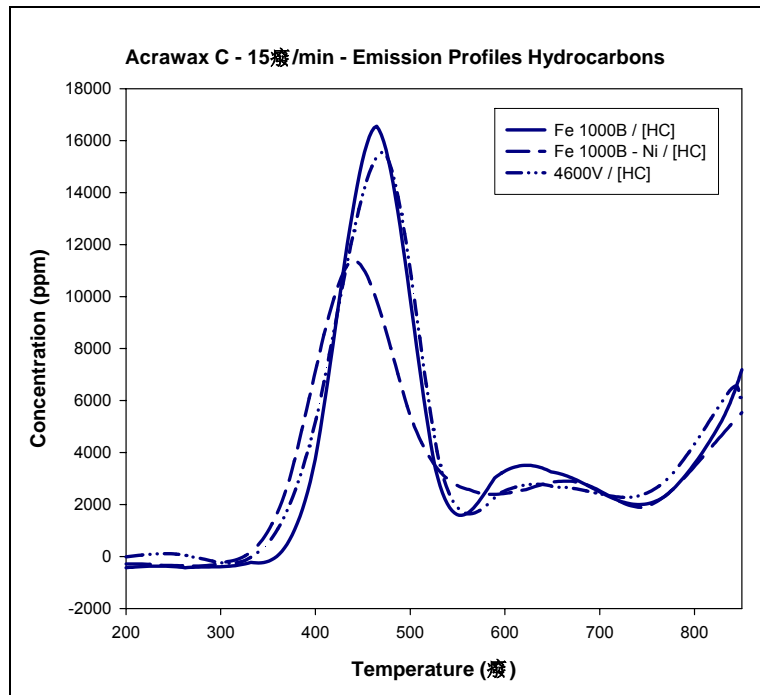
Figure 33. Hydrocarbons IR emission profiles. Acrawax C-lubricated samples [15°C/min].
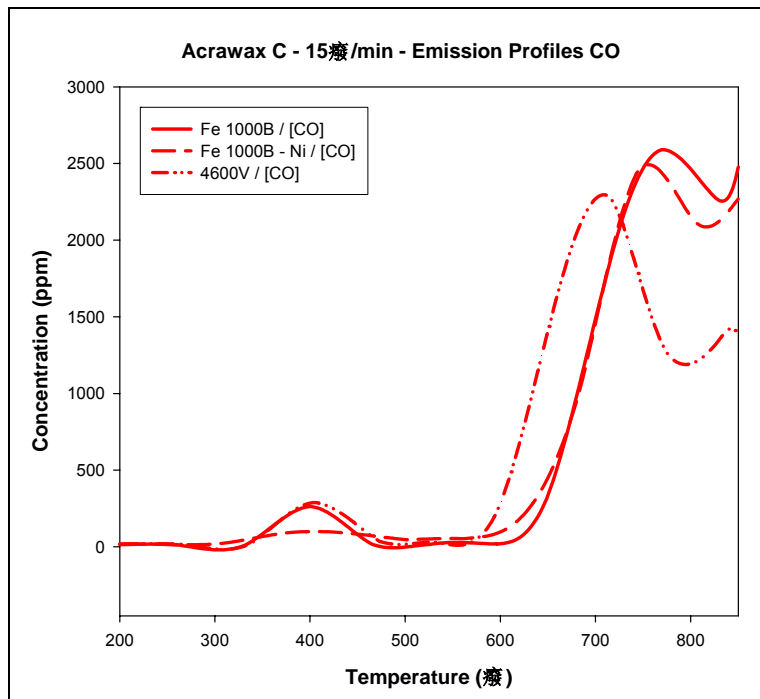
Figure 34. Carbon Monoxide IR emission profiles. Acrawax C-lubricated samples [15°C/min].

3.4.3.1 Formation of hydrocarbons

General observations.

The yields of hydrocarbons formed during pyrolysis were measured *in vivo* using IR spectroscopy. The results obtained in the present study are in line with the results from previous studies [9, 13]. As expected, a significant release of species with a pronounced hydrocarbon absorption band occurs for temperatures in the range of 450°C to 500°C. Under almost all processing conditions (*Figures 23, 25 and 27*) a secondary release of hydrocarbons takes place at higher temperatures. An explanation for this late release of hydrocarbons is given below.

Since IR spectroscopy cannot separate hydrocarbons in mixture (see above), the measured values correspond to the total amount of hydrocarbons in the gas mixture. The time dependencies of hydrocarbons formation during EBS pyrolysis measured with different heating rates, and for three different alloy composition are presented on *Figures 23, 25, 27, 29, 31 and 33*. In all cases, a bimodal formation of hydrocarbons is observed. A first strong emission of hydrocarbons occurs around the delubrication temperature (ca. 450°C) [9, 10], while a second, less reproducible emission takes place at temperatures above 600°C.

Effect of nickel for different heating rates.

According to the data presented in these figures, a small effect of nickel on the formation of hydrocarbons products is observed at lower and higher heating rates. At the lowest heating rate (5°C/min), a difference is observed for the second mode of hydrocarbons emission. More specifically, the second mode of hydrocarbon emission, for both nickel-containing samples, is observed at a temperature lower than in the case of the nickel-free sample (ca. 100°C lower). At the highest heating rate (15°C/min), the first peak emission of hydrocarbons is affected by the presence of admixed nickel, and a lower yield of hydrocarbons is observed, in comparison with the emission profiles of the other two samples. Also, the relative contribution of the secondary hydrocarbons emission (at temperatures above 600°C) decreases as the heating rate increases.

<u>Effect of the heating rate, for all alloy compositions</u>

In agreement with the work of Baum et al. [9], the emission peak of hydrocarbons consistently takes place at a temperature close to 450°C, after correction for the convection time. While it was proved that the occurrence of the peak was insensitive to the delubrication atmosphere and sample preparation date, it now appears that a slight effect of the heating rate can be noticed (*Figures 23, 25 and 27*). Indeed, previous studies using thermogravimetric analysis (TGA) had already come to the conclusion that delubrication is delayed by increasing the heating rate of the furnace [10-12]. As the heating rate goes from 5°C/min to 15°C/min, the temperature at which the peak intensity of hydrocarbons is detected is shifted by ca. 30°C. In addition, the amount of species with a hydrocarbon absorption band released in the processing atmosphere tends to increase with increasing heating rates. Because of the known FTIR limitations in terms of quantitative analysis [28], we will only discuss here the relative concentrations of emitted gases. The difference is particularly obvious between 5°C/min and 10°C/min.

<u>Predominance of long-chain hydrocarbons in the infrared signal:</u>

The infrared spectrum obtained during calibration experiments performed with pure CH_4 shows a characteristic pattern in the range of 3140 to 3050 cm^{-1} (*Figure 35a*), accounting for 26.9% of the overall signal for pure CH_4, and which does not overlap with any other signal. During analysis of the infrared data resulting from the delubrication experiments, the presence of this typical pattern is monitored (*Figure 35b*). Moreover, the respective areas covered by the pure CH_4 signal and by the rest of the hydrocarbon signal (double peak observed between 3000cm-1 and 2800cm-1) are calculated with the software OMNIC. It appears that, throughout the experiments, the overall CH_4 signal contribution remains consistently below 10% of the overall hydrocarbons signal. Similarly, the contribution of the C_2H_4 signal to the overall hydrocarbons signal is monitored by following, as a function of temperature, the intensity of a characteristic C_2H_4 peak at 3060.646 cm^{-1}, which does not overlap with any other signal. Here, the C_2H_4 signal contribution to the overall hydrocarbons never exceeds a level of 5%. These data

51

seems to show that over 85% of the hydrocarbon signal observed during the experiments performed in this study can be attributed to hydrocarbons other than methane and ethylene. This would also imply that, under the present experimental conditions, only low levels of EBS conversion to CH_4 and C_2H_4 are achieved.
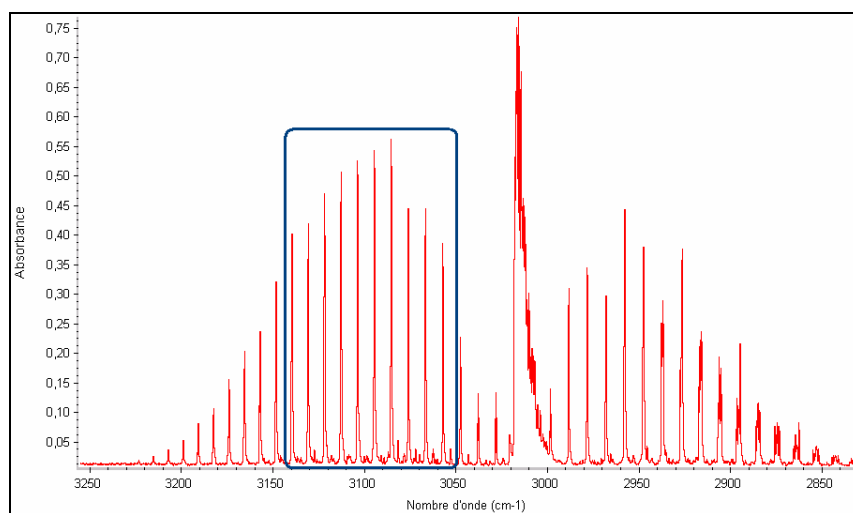
Figure 35a. Characteristic IR pattern of CH_4 during calibration experiment. $[CH_4]$=6170ppm. Flow rate = 2L.min-1. CH_4 peaks inside the blue box represent 26.9% of the overall CH_4 signal.
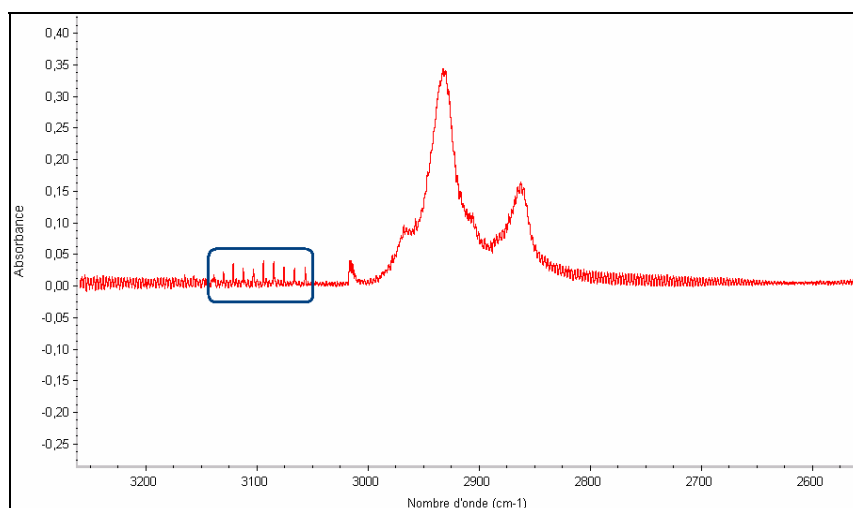
Figure 35b. Pyrolysis of Acrawax C at 10°C/min. Peak emission of CH_4 at 476°C. CH_4 signal represents 6.4% of the overall hydrocarbons signal at the temperature of CH_4 peak emission.

Similarities between the observed infrared spectra (in the 3000cm^{-1} to 2800cm^{-1} range) and the referenced infrared spectra of certain long-chain hydrocarbons.

The GC/MS results presented below prove that a series of long-chain hydrocarbons (alkanes and alkenes, mainly) were detected. Examination of the NIST database [30] shows that certain of these identified hydrocarbons (especially hexadecane, 1-hexadecene, pentadecane and 1-pentadecene) exhibit, in the 3000cm^{-1} to 2800cm^{-1} range, an infrared spectrum pattern very similar to the one observed throughout this study. This suggests that the hydrocarbon compounds mentioned above could account for most of the signal attributed to hydrocarbons, during the *in vivo* measurements. However, this is not in agreement with the quantitative measurements performed on the white solid product collected in the LN$_2$ trap (*Table 7a*).

Possible explanation for secondary emissions of hydrocarbons

The secondary emissions of hydrocarbons observed at higher temperatures (above 600°C) could be explained by possible condensation of EBS molecules (or other low volatile compounds resulting from the early stages of EBS decomposition) in the colder part of the setup. The fact that these secondary emissions tend to be more and more delayed with increasing heating rates (*Figures 23, 25 and 27*) would thus be consistent with the existence of a more pronounced non-uniformity of the temperature field inside the furnace in the case of the higher heating rates. Studying the boiling temperatures of the hydrocarbons identified by GC/MS measurements shows that all the alkanes/alkenes having more than 12 carbon atoms can potentially condense in the stainless steel connection line (maintained at 200°C), or in the cooler zones of the furnace, before evaporating, due to heat exchange with the hotter processing atmosphere. However, online infrared measurements of the secondary emissions of hydrocarbons did not provide any unambiguous evidence supporting this assumption.

Another explanation for this phenomenon is based on the assumption that the presence of nickel in the alloy composition enhances the cracking of the hydrocarbons chain of low volatile EBS decomposition by-products, which would be formed at temperatures below 500°C and temporarily remain inside the green compacts. As mentioned earlier, *Figures 23, 25 and 27* show

53

that the relative contribution of the secondary hydrocarbons emission to the overall hydrocarbons emission decreases with increasing heating rates. Thus, it can be concluded that the formation of EBS decomposition by-products prone to remaining temporarily inside of the compacts sample is a relatively slow reaction. This implies that a faster heating of the compacts leads to a more complete evaporation of EBS, with lower yields of low volatile products that remain in the samples even at temperatures above 500°C.

The decrease in hydrocarbons emission, in the case of nickel-containing samples, observed at higher heating rates means that some hydrocarbons are lost between reactor and IR cell. This can be explained if we suppose the formation of compounds containing hydrocarbons chains which condense in connection lines. This means that nickel, as an alloying element, is leading to the formation of less volatile compounds at temperatures from 450 to 500 °C.

Possible explanation for the effect of heating rate on the intensity of the first hydrocarbons peak emission.

A physical justification for this can be proposed. The flow rate of gases is kept constant during the whole set of experiments, and that the stainless steel connection line downstream is maintained at a lower temperature (200°C). This means that the by-products of lubricant pyrolysis, mainly emitted at the delubrication temperature, remain in the 'hot' zone of the furnace for an equal amount of time, regardless of the heating rate used. Thus, it can be suggested that the breakdown of these molecules into smaller hydrocarbons would be promoted, when exposed to post-delubrication temperatures (in the range of 450°C to 550°C).

3.4.3.2 Formation of carbon monoxide

General observations.

The yields of CO formed during EBS pyrolysis were also measured in this study. The emission profiles of CO measured as a function of temperature, for three different alloy compositions and with three different heating rates, are presented in *Figures 24, 26, 28, 30, 32*

and 34. The main feature of CO emission is the existence of a strong peak emission at high temperatures (generally above 700°C), which is in line with previous remarks [9].

Effect of the heating rate.

For the nickel-free sample, an increase in the heating rate, from 5 to 15°C/min, induces a strong drop in the amount of carbon monoxide produced at higher temperatures. However, the reverse trend is seen in the case of the sample containing admixed nickel: as the sample is heated faster, the overall yield of carbon monoxides increases. As opposed to these observations, the total amount of carbon monoxide produced by the sample containing prealloyed nickel is rather independent of the heating rate, even though the temperature at which the peak emission occurs tends to be shifted towards the higher temperatures, as the heating rate increases.

Effect of the presence of nickel.

At lower heating rates (5°C/min), a significant variation in the amount of CO produced is observed between nickel-containing and nickel-free samples, as the measured concentration of carbon monoxide is much higher in the case of nickel-free samples. This discrepancy between nickel-containing and nickel-free samples declines as the heating rate is increased. At higher heating rates (15°C/min), the levels of carbon monoxide produced by nickel-containing and nickel-free samples are comparable. A rationale for this phenomenon is provided below.

Gases that cannot be detected by infrared spectroscopy.

The formation of infrared-inactive gases cannot be excluded, especially H_2 formed from hydrocarbons. Potential formation of water would be masked by the background. Variations in the emission levels of CO_2 were detected. However, the significant background signal of CO_2 coming from the lab atmosphere did not allow for reasonable analysis of this data.

Potential Processes for CO formation

The observed important variations in the yields of CO for different heating rates can be attributed to a competition between the following two processes: **a.** CO formation and **b.** conversion of CO to CO_2.

The importance of these processes can be illustrated by the significantly higher concentration of CO produced by the nickel-free sample in the case of lower heating rate than in the case of the higher heating rate. This can explain why the heating rate has an impact on the amount of CO released at high temperatures, when the conversion reaction of CO to CO_2 is more effective.

$$\text{Sample} \rightarrow \text{CO, } (k_{obs})_1$$

$$\text{CO + Sample} \rightarrow CO_2, (k_{obs})_2$$
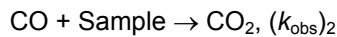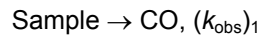
According to this scheme, the increasing value of $(k_{obs})_2$ relatively to $(k_{obs})_1$ is leading to a decrease in the measured amplitude of CO. A similar approach can be used in order to explain the low concentrations of CO produced, in the case of nickel-containing samples. In this case, a pseudo-catalytic formation of CO_2 from CO at lower temperatures can be assumed.

Two processes leading to the formation of carbon monoxide can be considered, when no Nickel is present inside of the compacts. Both processes involve formation of CO by reduction of the existing Fe oxides inside the compacts. It is even possible that the reduction of these oxides occurs simultaneously, and they can be written as follows:

$$\text{FeO + C = CO+ Fe} \qquad\qquad\qquad (1)$$

$$Fe_2O_3 + 3C = 3CO + 2Fe \qquad\qquad\qquad (2)$$

Thermodynamically, reaction path (1) for CO formation becomes favorable above 720°C, whereas path (2) is already active for temperatures above 620°C (*Figure 36*) [29].
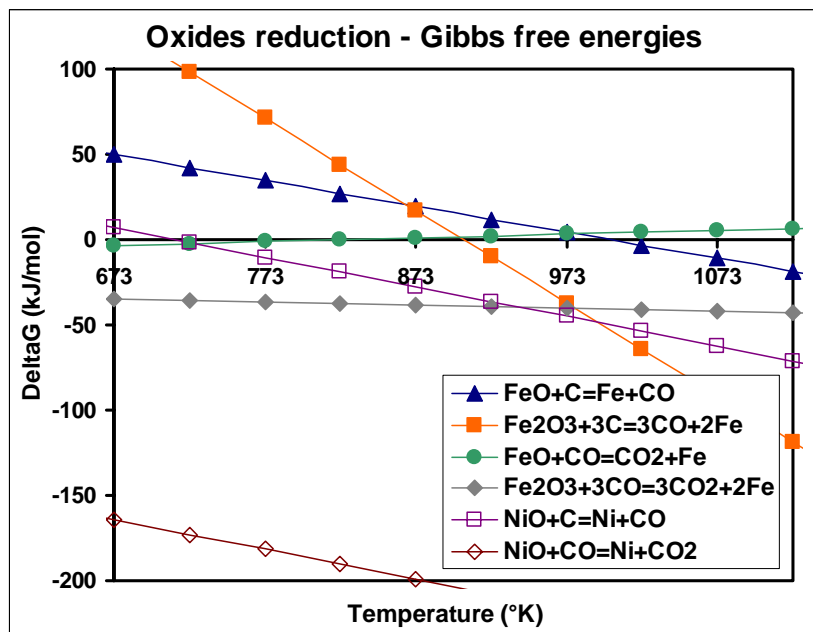
Figure 36. Gibbs free energies for the reduction of iron and nickel oxides.

In addition, this formation of CO can potentially promote the further reduction of FeO and Fe_2O_3 above 700°C, yielding carbon dioxide, as accounted for by reactions (3) and (4). Thermodynamic considerations show that pathway (3) is no longer favorable at temperatures above 600°C. However, pathway (4) is indeed active over the whole range of temperatures covered during the experiments (*Figure 36*) [29]. This implies that, if the heating rate inside the furnace is high, the formation of CO will be followed by a subsequent formation of CO_2. In other terms, a faster heating would lead to a higher conversion rate of carbon monoxide to carbon dioxide, which would be in line with certain observed decreases in the CO emission levels, as the heating rate goes up (*Figure 24*). Unfortunately, the strong CO_2 background coming from the lab atmosphere does not allow a valid interpretation of the CO_2 data.

$$FeO + CO = CO_2 + Fe \qquad\qquad\qquad (3)$$

$$Fe_2O_3 + 3CO = 3CO_2 + 2Fe \qquad\qquad\qquad (4)$$
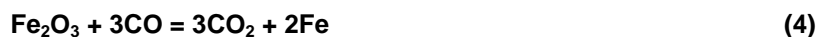
In the presence of Nickel, carbon monoxide can also be potentially formed via reduction of the Nickel oxides, according to the reaction:

$$NiO + C = Ni + CO \qquad\qquad\qquad (5)$$

57

Reaction (5) becomes thermodynamically favorable above 440°C (i.e. 10°C below the estimated delubrication temperature) [29]. Indeed, *Figures 24 and 26* show that, as we pass on from a Nickel-free system to a Nickel-containing system, the maximum intensity of the CO peak observed between 400°C and 450°C increases. Nevertheless, the temperature window over which this preliminary CO release takes place is somewhat too low to be conclusively attributed to an activation of the Nickel oxides reduction. However, slight uncertainties in the temperature measurements (due to temperature gradients between the tip of the K-thermocouple and the sample) might allow us to not rule out this possible mechanism. Lastly, no increase in the CO emission levels were observed in the case of the prealloyed Nickel-containing samples delubrication, when compared to that of the Nickel-free samples. We do not have a solid explanation for this discrepancy.

Similarly to what was proposed with reactions (3) and (4) in the case of the iron oxides, further reduction of the Nickel oxides can occur through reaction (6), which would thus be another pathway for the formation of carbon dioxide:

$$NiO + CO = Ni + CO_2 \qquad\qquad (6)$$

Thermodynamics prove that this reaction is favorable over the whole range of temperature covered during the experiments [29].

3.5 Conclusions

The results of this study confirm that the emission profiles observed upon heating of the compacts are affected by both the heating rate utilized, and by the alloy composition of the P/M component. More importantly, the possibility of gas sensor development is viable since the variations observed are not critical. Indeed, the characteristic features of lubricant pyrolysis, namely hydrocarbon and carbon monoxide peak emissions, are retained under all processing conditions investigated. The deviations observed, as the processing conditions were changed, can generally be accounted for; through GC/MS measurements it was confirmed that numerous chemical compounds were produced, and that the yield of these compounds depend on the processing conditions applied.

3.6 References

[1] German, R.M., *Powder Metallurgy Science*. 1984, Princeton, N.J.: Metal Powder Industries Federation. viii, 279.

[2] German, R.M., *Powder Metallurgy & Particulate Materials Processing*. 2005, Princeton, N.J.: Metal Powder Industries Federation. 528.

[3] Nayar, H.S. *Delubrication problems & solutions in the P/M industry*. In Proceedings of the 1994 International Conference & Exhibition on Powder Metallurgy & Particulate Materials. Part 3 (of 7), May 8-11 1994. 1994. Toronto, Can: Metal Powder Industries Federation, Princeton, NJ, USA.

[4] Takata, Z., H. Takigawa, and N. Kawai, *Behavior of dimensional change in sintering of Fe-based powders.* KOBELCO Technology Review, 1990(9): p. 5-9.

[5] Samal, P.K., *Factors affecting corrosion resistance of powder metal (P/M) stainless steels.* Key Engineering Materials. 2nd International Latin-American Conference on Powder Technology, 2001. **189-191**: p. 328-339.

[6] Legzdins, C.F., I.V. Samarasekera, and T. Troczynski, *A comparative study of delubrication and associated defects for high temperature sintered ferrous materials.* Advances in Powder Metallurgy and Particulate Materials, 1999. **1**: p. 3-57-3-72.

[7] Legzdins, C.F., I.V. Samarasekera, and T. Troczynski. Experimental studies of Zinc stearate delubrication in high temperature sintering of ferrous compacts. In PM Tech. 1999. Vancouver, BC.

[8] White, G.R. and H. Nayar, *Monitoring and control of delubrication under production conditions*. 1996, Metal Powder Industries Federation: Princeton, N.J. p. 10-27-10-40.

[9] Baum, M.M., et al., *Lubricant pyrolysis during sintering of powder metallurgy compacts*. Metallurgical and Materials Transactions B: Process Metallurgy and Materials Processing Science, 2004. **35**(2): p. 381-392.

[10]Saha, D. and D. Apelian, *Control strategy for de-lubrication of P/M compacts.* International Journal of Powder Metallurgy (Princeton, New Jersey), 2002. **38**(3): p. 71-79.

[11]Saha, D., *Delubrication during sintering of P/M compacts: Operative mechanism and process control strategy*, in Materials Science and Engineering. 2001, Worcester Polytechnic Institute: Worcester, MA. p. 120.

[12]Saha, D. and D. Apelian. *Optimization of delubrication during sintering*, in International Conference on Powder Metallurgy & Particulate Materials. 2000. New York, NY, USA.

[13]Saha, D., M.M. Baum, and D. Apelian. *Mechanism of de-lubrication during sintering: Reaction kinetics and decomposition stages*, in Advances in Powder Metallurgy and Particulate Materials - 2001, May 13-17 2001. 2001. New Orleans, LA, United States: Metal Powder Industries Federation.

[14]Phillips, M.A., P. Pourtalet, and I. Lampre. *Removal of lubricants from P/M tool steels and stainless steels*, in Proceedings of the 1993 International Conference and Exhibition on Powder Metallurgy and Particulate Materials, May 16-19 1993. 1993. Nashville, TN, USA: Publ. by Metal Powder Industries Federation, Princeton, NJ, USA.

[15]Hwang, K.-S. and K.-H. Lin, *Lubricant removal in metal powder compacts.* International Journal of Powder Metallurgy (Princeton, New Jersey), 1992. **28**(4): p. 7.

[16]Renowden, M. and P. Pourtalet. *Experimental studies on lubricant removal*, in Proceedings of the 1990 Powder Metallurgy Conference and Exhibition Part 1 (of 3), May 20-23 1990.

1990. Pittsburgh, PA, USA: Publ by Metal Powder Industries Federation, Princeton, NJ, USA.

[17]White, G.R., A. Griffo, and H. Nayar. *Effect of atmosphere additions on increasing delubing efficiency on Fe-2Cu-0.8C*, in Proceedings of the 1994 International Conference & Exhibition on Powder Metallurgy & Particulate Materials. Part 3 (of 7), May 8-11 1994. 1994. Toronto, Can: Metal Powder Industries Federation, Princeton, NJ, USA.

[18]Dwyer, J., et al. *Comparative studies of P/M lubricants under different atmospheres using TGA techniques,* in Proceedings of the 1992 Powder Metallurgy World Congress. Part 3 (of 9), Jun 21-26 1992. 1992. San Francisco, CA, USA: Publ by Metal Powder Industries Federation, Princeton, NJ, USA.

[19]Poskrebyshev, G.A., et al. *Mechanism of N,N'-ethylenebisstearamide pyrolysis and formation of CO, CO2, CH4 and C2H4 of in the presence of iron/carbon powder under vacuum at 300C < T < 700C*. In 229th American Chemical Society National Meeting & Exposition. 2005. San Diego, CA.

[20]Nakano, H., et al., *Carbon deposition by disproportionation of CO on a Ni(977) surface.* Surface Science, 2000. **Vol. 454-456**: p. pp. 295-299.

[21]Park, C., N.M. Rodriguez, and R.T.K. Baker, *Carbon Deposition on Iron-Nickel during Interaction with Carbon Monoxide-Hydrogen Mixtures*. Journal of Catalysis, 1997. **169**(1): p. 212.

[22]Park, C. and R.T.K. Baker, *Carbon Deposition on Iron-Nickel during Interaction with Ethylene-Hydrogen Mixtures*. Journal of Catalysis, 1998. **179**: p. 361-374.

[23]Bin, Y., et al., *Catalytic effect of nickel under carbonization of polyimide films*. Carbon, 2005. **43**(8): p. 1617-1627.

[24]Morozova, O.S., et al., *Effect of initial nickel and iron oxide morphology on their structural transformation in CO/H2 mixture*. Catalysis Today, 1997. **33**(1-3): p. 323-334.

[25]Marginean, P. and A. Olariu, *Influence of metal oxides on the catalytic activity of nickel.* Applied Catalysis A: General, 1997. **165**(1-2): p. 241-248.

[26]Sutton, D., et al., *Investigation of nickel supported catalysts for the upgrading of brown peat derived gasification products*. Bioresource Technology, 2001. **80**(2): p. 111-116.

[27]Celina, M., et al., *FTIR emission spectroscopy applied to polymer degradation.* Polymer Degradation and Stability, 1997. **58**(1-2): p. 15-31.

[28]Gaskell, D.R., *Introduction to the thermodynamics of materials*. 3rd ed. 2003, New York, NY: Taylor & Francis.

[29]NIST, NIST Chemistry WebBook. *http://webbook.nist.gov/chemistry/*

[30]Markley, K.S., *Fats and Oils*, in *Hydrogenation*, Interscience, Editor. 1961, Markley K.S.: New York, NY. p. pp. 1187-1305.

[31]Figoli N. S., B.J.N., Ouerini C. A. and Parera J. M., *Measurement of activity decay of naphtha reforming catalyst.* Applied Catalysis, 1985. **15**(1): p. 41-47.

4.0 Future Work

Further study of the mechanisms of delubrication should involve, if possible, a validation of the mathematical empirical model for heavier parts, and if not computer simulation of the weight loss behavior for massive components. Previous studies having showed that T_{MAX} closely matches the temperature of hydrocarbons peak emission from the parts (FTIR experiments), experiments should be performed in order to validate this statement for increasing parts weights. The dependencies of T_{MAX} and b should also be tested for a broader range of S/V values.

Also, the origin of the CO and CO_2 emissions at high temperatures should be clearly established, as well as its potential link with decarburization of the parts. A first step would then be to perform similar delubrication experiments with graphite-containing and graphite-free parts, combined with online FTIR measurements.

5.0 Appendix: unidentified mass spectra

"A abs." stands for absolute intensity of the corresponding peak on the chromatogram of A, and is given in number of counts.
"A %" stands for relative intensity of the corresponding peak on the chromatogram of A, and is given in percentage.
Intensities in the chromatograms are given for the sample D.

The retention times ("Ret.Time") are given in minutes.

Ret.Time	A abs.	A %	B abs.	B %	C abs.	C %	D abs.	D %	E abs.	E %	F abs.	F %
37,263	274067	2,65	170413	1,91	400035	5,13	1664693	31,3	82010	0,73	116586	1,47

Retention time: 37.26 min
# of Peaks   76
Raw Spectrum   37.263 -> 37.263 (scan: 13706 -> 13706)
Background   No Background Spectrum
Base Peak   m/z 267.45 (Intensity: 183,898)

Background MS
34.705-35.54

Ret.Time	A abs.	A %	B abs.	B %	C abs.	C %	D abs.	D %	E abs.	E %	F abs.	F %
29,353	134631	1,3	178820	2	138238	1,77	2120900	39,9	74974	0,66	168381	2,12

Retention time: 29.325 min
# of Peaks 91
Raw Spectrum 29.353 -> 29.353
(scan: 10542 -> 10542)
No Background Spectrum
Base Peak m/z 56.90 (Intensity: 188,644)

Ret.Time	A abs.	A %	B abs.	B %	C abs.	C %	D abs.	D %	E abs.	E %	F abs.	F %
28,303	693607	6,71	797940	8,93	746374	9,58	495459	9,31	311675	2,76	589283	7,43

Retention time: 28.3 min
# of Peaks 55
Raw Spectrum 28.303 -> 28.303 (scan: 10122 -> 10122)
No Background Spectrum
Base Peak m/z 82.05 (Intensity: 128,296)

Ret.Time	A abs.	A %	B abs.	B %	C abs.	C %	D abs.	D %	E abs.	E %	F abs.	F %
27,71	10336693	100	6606724	74	7753037	99,5	5188967	97,5	11292464	100	6867961	86,6

Retention time: 27.71 min
# of Peaks 67
Raw Spectrum 27.710 -> 27.710 (scan: 9885 -> 9885)
No Background Spectrum
Base Peak m/z 84.15 (Intensity: 1,875,308)

64

Ret.Time	A abs.	A %	B abs.	B %	C abs.	C %	D abs.	D %	E abs.	E %	F abs.	F %
25,91	7860706	76,1	4577343	51,3	6360574	81,6	4591628	86,3	10241558	90,7	6655889	83,9

Retention time: 25.9 min
# of Peaks   51
Raw Spectrum   25.910 -> 25.910 (scan: 9165 -> 9165)
No Background Spectrum
Base Peak   m/z 84.20 (Intensity: 1,697,102)

Ret.Time	A abs.	A %	B abs.	B %	C abs.	C %	D abs.	D %	E abs.	E %	F abs.	F %
26,538	727817	7,04	297495	3,33	884944	11,4	407024	7,65	402276	3,56	336823	4,24

Retention time: 26.5 min
# of Peaks   31
Raw Spectrum   26.538 -> 26.538 (scan: 9416 -> 9416)
No Background Spectrum
Base Peak   m/z 82.05 (Intensity: 103,237)

Ret.Time	A abs.	A %	B abs.	B %	C abs.	C %	D abs.	D %	E abs.	E %	F abs.	F %
26,83	228852	2,21	219948	2,46	245753	3,15	146587	2,76	246675	2,18	188616	2,38

Retention time: 26.8 min
# of Peaks   17
Raw Spectrum   26.830 -> 26.830 (scan: 9533 -> 9533)
No Background Spectrum
Base Peak   m/z 84.20 (Intensity: 44,454)

65

Ret.Time	A abs.	A %	B abs.	B %	C abs.	C %	D abs.	D %	E abs.	E %	F abs.	F %
23,898	1092049	10,6	1317341	14,8	1563725	20,1	**2099973**	**39,5**	2012797	17,8	2034084	25,6

Retention time: 23.9 min
# of Peaks   66
Raw Spectrum   23.898 -> 23.898 (scan: 8360 -> 8360)
No Background Spectrum
Base Peak   m/z 56.90 (Intensity: 268,723)

Ret.Time	A abs.	A %	B abs.	B %	C abs.	C %	D abs.	D %	E abs.	E %	F abs.	F %
23,963	217501	2,1	512343	5,74	312584	4,01	**337231**	**6,34**	323103	2,86	497975	6,28

Retention time: 23.96 min
# of Peaks   25
Raw Spectrum   23.963 -> 23.963 (scan: 8386 -> 8386)
No Background Spectrum
Base Peak   m/z 84.20 (Intensity: 128,721)

Ret.Time	A abs.	A %	B abs.	B %	C abs.	C %	D abs.	D %	E abs.	E %	F abs.	F %
23,843	298827	2,89	214430	2,4	353412	4,54	**287520**	**5,4**	470380	4,17	333950	4,21

Retention time: 23.8 min
# of Peaks   22
Raw Spectrum   23.843 -> 23.843 (scan: 8338 -> 8338)
No Background Spectrum
Base Peak   m/z 57.75 (Intensity: 81,377)

66

Ret.Time	A abs.	A %	B abs.	B %	C abs.	C %	D abs.	D %	E abs.	E %	F abs.	F %
21,773	336974	3,26	507533	5,68	516968	6,64	703221	13,2	581978	5,15	701097	8,84

Retention time: 21.77 min
# of Peaks 42
Raw Spectrum 21.773 -> 21.773 (scan: 7510 -> 7510)
No Background Spectrum
Base Peak m/z 96.70 (Intensity: 92,184)

Ret.Time	A abs.	A %	B abs.	B %	C abs.	C %	D abs.	D %	E abs.	E %	F abs.	F %
21,94	8179	0,08	12514	0,14	23373	0,3	67124	1,26	66316	0,59	78428	0,99

Retention time: 21.9 min
# of Peaks 18
Raw Spectrum 21.940 -> 21.940 (scan: 7577 -> 7577)
No Background Spectrum
Base Peak m/z 57.05 (Intensity: 10,045)

Ret.Time	A abs.	A %	B abs.	B %	C abs.	C %	D abs.	D %	E abs.	E %	F abs.	F %
21,66	10464	0,1	33334	0,37	13633	0,17	59839	1,12	34699	0,31	37405	0,47

Retention time: 21.66 min
# of Peaks 22
Raw Spectrum 21.660 -> 21.660
(scan: 7465 -> 7465)
No Background Spectrum
Base Peak m/z 57.05 (Intensity: 6,618)

67

Ret.Time	A abs.	A %	B abs.	B %	C abs.	C %	D abs.	D %	E abs.	E %	F abs.	F %
33,18	139371	1,35	98739	1,11	186125	2,39	587903	11,1	95406	0,84	59046	0,74

Retention time: 33.18 min
# of Peaks 54
Raw Spectrum   33.180 -> 33.180 (scan: 12073 -> 12073)
No Background Spectrum
Base Peak   m/z 87.05 (Intensity: 166,227)

Ret.Time	A abs.	A %	B abs.	B %	C abs.	C %	D abs.	D %	E abs.	E %	F abs.	F %
32,883	135967	1,32	102875	1,15	229423	2,94	610200	11,5	85494	0,76	68803	0,87

Retention time: 32.88 min
# of Peaks 60
Raw Spectrum   32.883 -> 32.883 (scan: 11954 -> 11954)
No Background Spectrum
Base Peak   m/z 87.05 (Intensity: 141,113)

Ret.Time	A abs.	A %	B abs.	B %	C abs.	C %	D abs.	D %	E abs.	E %	F abs.	F %
19,433	70347	0,68	85630	0,96	95136	1,22	110060	2,07	125211	1,11	126821	1,6

Retention time: 19.43 min
# of Peaks 19
Raw Spectrum   19.433 -> 19.433 (scan: 6574 -> 6574)
No Background Spectrum
Base Peak   m/z 57.05 (Intensity: 11,467)

68

Ret.Time	A abs.	A %	B abs.	B %	C abs.	C %	D abs.	D %	E abs.	E %	F abs.	F %
19,383	382611	3,7	755361	8,46	577645	7,41	**681964**	**12,8**	891367	7,89	991302	12,5

Retention time: 19.38 min
# of Peaks   21
Raw Spectrum   19.383 -> 19.383 (scan: 6554 -> 6554)
No Background Spectrum
Base Peak   **m/z 56.95** (Intensity: 216,044)

Ret.Time	A abs.	A %	B abs.	B %	C abs.	C %	D abs.	D %	E abs.	E %	F abs.	F %
19,308	87858	0,85	263891	2,95	167593	2,15	**284106**	**5,34**	217862	1,93	374616	4,72

Retention time: 19.31 min
# of Peaks   19
Raw Spectrum   19.308 -> 19.308
                        (scan: 6524 -> 6524)
No Background Spectrum
Base Peak   **m/z 54.85** (Intensity: 36,547)

Ret.Time	A abs.	A %	B abs.	B %	C abs.	C %	D abs.	D %	E abs.	E %	F abs.	F %
18,15	411772	3,98	546266	6,12	614404	7,89	**509939**	**9,58**	853180	7,56	772954	9,74

Retention time: 18.15 min
# of Peaks   21
Raw Spectrum   18.150 -> 18.150 (scan: 6061 -> 6061)
No Background Spectrum
Base Peak   **m/z 56.95** (Intensity: 166,549)

69

Ret.Time	A abs.	A %	B abs.	B %	C abs.	C %	D abs.	D %	E abs.	E %	F abs.	F %
18,063	516293	4,99	634876	7,11	811619	10,4	590606	11,1	956802	8,47	879912	11,1

Retention time: 18.06 min
# of Peaks   22
Raw Spectrum   18.063 -> 18.063 (scan: 6026 -> 6026)
No Background Spectrum
Base Peak   m/z 54.75 (Intensity: 73,636)

Ret.Time	A abs.	A %	B abs.	B %	C abs.	C %	D abs.	D %	E abs.	E %	F abs.	F %
16,858	164993	1,6	692753	7,76	283678	3,64	549602	10,3	420721	3,73	852969	10,8

Retention time: 16.85 min
# of Peaks   18
Raw Spectrum   16.858 -> 16.858 (scan: 5544 -> 5544)
No Background Spectrum
Base Peak   m/z 56.95 (Intensity: 195,711)

Ret.Time	A abs.	A %	B abs.	B %	C abs.	C %	D abs.	D %	E abs.	E %	F abs.	F %
16,76	226797	2,19	547013	6,13	328199	4,21	473573	8,9	420028	3,72	745628	9,4

Retention time: 16.76 min
# of Peaks   18
Raw Spectrum   16.760 -> 16.760
                        (scan: 5505 -> 5505)
No Background Spectrum
Base Peak   m/z 54.75 (Intensity: 65,324)

70

Ret.Time	A abs.	A %	B abs.	B %	C abs.	C %	D abs.	D %	E abs.	E %	F abs.	F %
15,463	484507	4,69	319528	3,58	742924	9,54	**351448**	**6,61**	849423	7,52	469309	5,91

Retention time: 15.46 min
# of Peaks   19
Raw Spectrum   15.463 -> 15.463 (scan: 4986 -> 4986)
No Background Spectrum
Base Peak   m/z 56.95 (Intensity: 130,408)

Ret.Time	A abs.	A %	B abs.	B %	C abs.	C %	D abs.	D %	E abs.	E %	F abs.	F %
15,363	229337	2,22	328440	3,68	402362	5,16	**365452**	**6,87**	410705	3,64	488773	6,16

Retention time: 15.36 min
# of Peaks   19
Raw Spectrum   15.363 -> 15.363
                          (scan: 4946 -> 4946)
No Background Spectrum
Base Peak   m/z 54.80 (Intensity: 51,243)

Ret.Time	A abs.	A %	B abs.	B %	C abs.	C %	D abs.	D %	E abs.	E %	F abs.	F %
13,998	260726	2,52	344691	3,86	451257	5,79	**442464**	**8,32**	520839	4,61	604461	7,62

Retention time: 13.998 min
# of Peaks   18
Raw Spectrum   13.998 -> 13.998 (scan: 4400 -> 4400)
No Background Spectrum
Base Peak   m/z 56.95 (Intensity: 173,376)

71

Ret.Time	A abs.	A %	B abs.	B %	C abs.	C %	D abs.	D %	E abs.	E %	F abs.	F %
13,88	191317	1,85	252997	2,83	303085	3,89	326703	6,14	342511	3,03	466790	5,88

Retention time: 13.88 min
# of Peaks   19
Raw Spectrum   13.880 -> 13.880 (scan: 4353 -> 4353)
No Background Spectrum
Base Peak   m/z 54.85 (Intensity: 46,125)

Ret.Time	A abs.	A %	B abs.	B %	C abs.	C %	D abs.	D %	E abs.	E %	F abs.	F %
12,413	282427	2,73	208917	2,34	436254	5,6	339154	6,37	513621	4,55	407447	5,14

Retention time: 12.4 min
# of Peaks   17
Raw Spectrum   12.413 -> 12.413 (scan: 3766 -> 3766)
No Background Spectrum
Base Peak   m/z 56.95 (Intensity: 136,886)

Ret.Time	A abs.	A %	B abs.	B %	C abs.	C %	D abs.	D %	E abs.	E %	F abs.	F %
12,288	124183	1,2	206837	2,32	192052	2,47	299094	5,62	211172	1,87	390886	4,93

Retention time: 12.29 min
# of Peaks   16
Raw Spectrum   12.288 -> 12.288 (scan: 3716 -> 3716)
No Background Spectrum
Base Peak   m/z 54.75 (Intensity: 54,617)

Ret.Time	A abs.	A %	B abs.	B %	C abs.	C %	D abs.	D %	E abs.	E %	F abs.	F %
10,703	217775	2,11	310445	3,48	339075	4,35	**461634**	**8,68**	379992	3,37	426426	5,37

Retention time: 10.7 min
# of Peaks 13
Raw Spectrum 10.703 -> 10.703 (scan: 3082 -> 3082)
No Background Spectrum
Base Peak **m/z 56.95** (Intensity: 208,645)

Ret.Time	A abs.	A %	B abs.	B %	C abs.	C %	D abs.	D %	E abs.	E %	F abs.	F %
10,563	104778	1,01	351092	3,93	161564	2,07	**430197**	**8,09**	184017	1,63	478804	6,03

Retention time: 10.56 min
# of Peaks 19
Raw Spectrum 10.563 -> 10.563 (scan: 3026 -> 3026)
No Background Spectrum
Base Peak **m/z 54.80** (Intensity: 71,176)

Ret.Time	A abs.	A %	B abs.	B %	C abs.	C %	D abs.	D %	E abs.	E %	F abs.	F %
8,838	103623	1	348831	3,91	108421	1,39	**426898**	**8,02**	112249	0,99	392940	4,95

Retention time: 8.84 min
# of Peaks 11
Raw Spectrum 8.838 -> 8.838 (scan: 2336 -> 2336)
No Background Spectrum
Base Peak **m/z 56.90** (Intensity: 203,679)

Ret.Time	A abs.	A %	B abs.	B %	C abs.	C %	D abs.	D %	E abs.	E %	F abs.	F %
8,675	102784	0,99	418285	4,68	104665	1,34	**481322**	**9,05**	103284	0,91	506784	6,39

Retention time: 8.68 min
# of Peaks   17
Raw Spectrum   8.675 -> 8.675 (scan: 2271 -> 2271)
No Background Spectrum
Base Peak   **m/z 55.95** (Intensity: 88,220)

Ret.Time	A abs.	A %	B abs.	B %	C abs.	C %	D abs.	D %	E abs.	E %	F abs.	F %
6,793	175555	1,7	76207	0,85	244457	3,14	**179577**	**3,38**	214725	1,9	157443	1,98

Retention time: 6.79 min
# of Peaks   8
Raw Spectrum   6.793 -> 6.793 (scan: 1518 -> 1518)
No Background Spectrum
Base Peak   **m/z 56.90** (Intensity: 86,796)

Ret.Time	A abs.	A %	B abs.	B %	C abs.	C %	D abs.	D %	E abs.	E %	F abs.	F %
6,635	60391	0,58	168646	1,89	72218	0,93	**271869**	**5,11**	61654	0,55	372766	4,7

Retention time: 6.63 min
# of Peaks   15
Raw Spectrum   6.635 -> 6.635 (scan: 1455 -> 1455)
No Background Spectrum
Base Peak   **m/z 56.00** (Intensity: 67,362)

74